Theory of magnetoplasmon excitations in Rashba spintronic quantum wires: Maxons, rotons, and negative-energy dispersion

Manvir S. Kushwaha
Institute of Physics, University of Puebla, P.O. Box J-45, Puebla 72570, Mexico
(Received 29 December 2006; revised manuscript received 4 October 2007; published 14 December 2007)

We report on the theoretical investigation of plasmon excitations in a quasi-two-dimensional electron gas in the presence of a harmonic potential (oriented along the x direction), an applied perpendicular (to the x-y plane) magnetic field, and the spin-orbit interaction (SOI) induced by the Rashba effect. The resultant system is a quasi-one-dimensional (Q1D) quantum wire with free propagation along the y direction and magnetoelectric quantization along the x. The problem involves three length scales: $l_0=\sqrt{\hbar/m^*\omega_0}$, $l_c=\sqrt{\hbar/m^*\omega_c}$, and $l_\alpha=\hbar^2/(2m^*\alpha)$, which characterize the relative strengths in the interplay of confinement, the magnetic field, and the Rashba SOI. The resulting Schrödinger-like equations satisfied by the wave function (accounting for the spin-up and spin-down states) are two coupled equations, which cannot be solved in an explicit analytical form. However, invoking the limits of a strong magnetic field, $l_c \ll l_0$, and $k_y l_0 \ll 1$ allows us to solve this set of coupled equations exactly. We then derive and discuss the dispersion relations for charge-density excitations within the framework of Bohm-Pines' random-phase approximation. The intrasubband and intersubband magnetoplasmons in a Q1D electron gas are characterized, respectively, by the negative-energy dispersion with increasing magnetic field and the magnetoroton excitation which changes its group velocity twice before merging with the respective single-particle continuum. Here we scrutinize the effect of the Rashba SOI on these characteristics in depth. We observe that the SOI modifies drastically the behavior of both the intrasubband and intersubband magnetoplasmons in the long-wavelength limit and may render them relatively more susceptible to the Landau damping in the short-wavelength limit. We discuss the dependence of the magnetoplasmon energy on the propagation vector, the magnetic field, the 1D charge density, and the Rashba parameter characterizing the SOI.

DOI: 10.1103/PhysRevB.76.245315 PACS number(s): 71.70.Ej, 72.25.Dc, 73.21.Hb, 73.43.Lp

I. INTRODUCTION

Thanks to advances in high-resolution lithography and controlled-growth techniques, it is now possible to make semiconductor devices that allow the distribution of free electrons to be squeezed into any desired shape and size. As a consequence of this technological progress, the semiconducting systems can now be made with such purity that electrons can flow inside them without being scattered (by any imperfections or impurities) at all, i.e., ballistically. This has triggered an increasingly active field in the condensed matter physics—the so-called physics of the systems of reduced dimensionality—during the past two decades. The dimensionality in this context refers to the number of degrees of freedom of the electron momentum. The current trend in physics and fabrication of man-made nanostructures is stimulated by the worldwide quest to develop exotic high-speed, low-power devices that are small enough, sharp enough, or uniform enough to behave the way theory says they should. These are quantum structures known as quantum wells, quantum wires, and quantum dots—in which charge carriers exhibit quantum effects that strongly modify their behavior.[1]

The remarkable progress made on the miniaturization (of size and dimensions) has in recent years focused onto the study of the narrow-gap semiconductors, most notably InAs, and the important role they play in the rapidly evolving field of *spintronics*.[2] As a nonmagnetic element in hybrid devices, these semiconducting materials are expected to help us control the electron spin states just as the electron charge is controlled in the conventional electronic devices. The main idea behind such devices is that the spin-orbit interaction (SOI) in the narrow-gap semiconductors causes the spins of the carriers to precess. This was proposed by Datta and Das in a classic paper,[3] which describes how the external gate electrode can be used to manipulate the SOI provided that the latter depends on the interface electric field, the so-called Rashba effect.[4] This is a gate-voltage-induced spin splitting of band edge states in the absence of an applied magnetic field and can be enhanced further by increasing the gate voltage.

Recent years have seen a tremendous research interest in the spin dynamics associated with the emerging field of spintronics.[2] Spintronics is based in part on manipulation of the spin degree of freedom of the carriers to develop features and functionalities for solid state devices. Basic design proposals for spintronic devices with a wide range of applications, such as spin field-effect transistors,[3] biological sensing,[5] quantum computing,[6] field-effect switches,[7] spin filters,[8] data storage,[9] etc., rely on the fact that electron waves with opposite spin acquire a phase difference during their propagation in the presence of the Rashba effect. It is noteworthy that vast majority of research efforts in spintronics are still confined to the studies of the influence of the Rashba SOI on the electronic, optical, and transport properties in quasi-two-dimensional electron gas.[10] An interesting question is as follows. How the Rashba SOI is manifested in still lower-dimensional systems such as quasi-one-dimensional electron gas (Q1DEG) or quantum wires?

The quantum wires lie midway of the quantum rainbow and are known to possess some unique transport properties

such as magnetic depopulation,[11] electron waveguide,[12] quenching of the Hall effect,[13] quantization of conductance,[14] negative-energy dispersion,[15] magnetoroton excitations,[16] spin-charge separation,[17] to name a few. The theoretical investigations on the quantum wires, particularly associated with the magnetoplasmon excitations,[18–20] have not been, due in part to the mathematical complexity, quite consistent with the experimental findings. For instance, no theoretical work[18,20] has, to our knowledge, been able to verify the prediction of the existence of magnetorotons[19] in quantum wires in the presence of an applied perpendicular magnetic field. Also, our understanding of the inter-Landau level collective excitations in quantum wires has been quite limited in the situations where Kohn's theorem[21] is violated. As to the investigation of the effect of the Rashba SOI and the (perpendicular) magnetic field on the electronic and transport properties of the quantum wires, the situation is still in its infancy and only a few elementary theoretical papers on the energy band structures[22–24] and spin Hall effect,[25] and the experimental work on the magnetotransport[26] have just started appearing. To what extent these (combined) effects can influence the behavior of the plasmon excitations in quantum wires has, to our knowledge, not been investigated, and this is the aim of the present work.

One of the main motivations behind the present study is the suggestion that the zero-field spin splitting of electron bands could catalyze experiments on quantum-wire-based devices that exploit both the charge and spin of an electron, e.g., active spin polarizer[27] and spin transistors.[28] Therefore, it seems worthwhile to explore the electron spin dynamics as a possible route toward the fundamental understanding of the magnetotransport phenomena in quantum wires in the presence of an applied (perpendicular) magnetic field. To be specific, we investigate here the magnetoplasmon excitations in $In_{1-x}Ga_xAs/In_{1-x}Al_xAs$ quantum wires subjected to a perpendicular (to the x-y plane) magnetic field and the SOI induced by the Rashba effect within the two-subband model with only the lowest one occupied in the framework of Bohm-Pines' random-phase approximation (RPA).[29] It is worth mentioning that we do not want to spend here on whether the realistic quantum wires (as is the case here) are better described as Fermi liquids or as Luttinger liquids. This is because we trust that this issue is already reliably settled (see, for details, Ref. 1) and we believe that the Fermi-liquid-like RPA formalism is justifiable by all means. Similar efforts to study the plasmon excitations in quantum wells—with zero[30] and finite[31] magnetic field—and in quantum wires—with zero[32] magnetic field—have brought to attention the importance and intricacies of the Rashba SOI.

The magnetoplasmon excitations in a Q1DEG (without the SOI) are known to possess the following interesting properties: (i) the negative dispersion with the increasing magnetic field—a behavior characteristic of the edge-plasmon-type oscillations whose frequencies are determined by the circumference of the samples,[33] and (ii) the intersubband magnetoplasmon exhibiting the roton minimum—an excitation proposed by Feynman in superfluid ^{4}He a long time ago.[34] The presence of the Rashba SOI and the applied (perpendicular) magnetic field in a quantum wire gives rise to three length scales in the problem: $l_0=\sqrt{\hbar/m^*\omega_0}$, $l_c=\sqrt{\hbar/m^*\omega_c}$, and $l_\alpha=\hbar^2/(2m^*\alpha)$, which characterize the relative strengths in the interplay of confinement, the magnetic field, and the Rashba SOI, respectively. This complicates the analytical diagnosis to the extent that the resulting coupled equations in terms of the wave function (accounting for the spin-up and spin-down states) cannot be solved in an explicitly analytical form. However, in the limit of $l_c \ll l_0$ and $k_y l_0 \ll 1$ we can solve this set of coupled equations exactly (see Sec. II below). We identify the former with a strong magnetic field and the latter (virtually) with a long-wavelength limit. As such, we are able to determine the eigenfunctions and eigenvalues required to employ the RPA and to develop the mathematical machinery to derive and discuss the general nonlocal, dynamical dielectric function needed to investigate the collective and single-particle excitations in quantum wires in the presence of the applied magnetic field and the Rashba SOI.

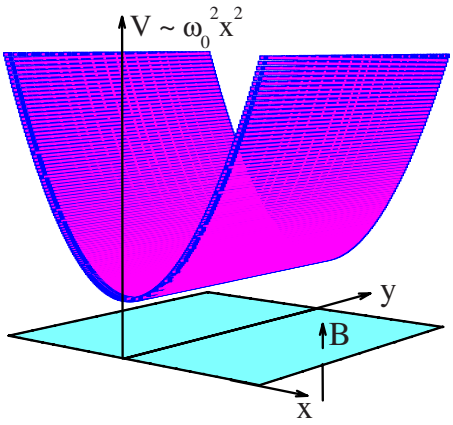

FIG. 1. (Color online) The model quantum wire investigated in this work.

The remainder of the article is organized as follows: Section II is the main part of the paper which is devoted to outline the mathematical machinery to obtain the solution of the problem and to the analytical diagnoses of the results obtained within the RPA. In other words, Sec. II is dedicated to discuss our mathematical formalism to derive the required nonlocal, dynamic dielectric function for the Q1DEG in the presence of an applied (perpendicular) magnetic field and the SOI due (wholly) to the Rashba mechanism. Section III is devoted to discuss several illustrative examples on the magnetoplasmon excitations for various case studies, including the results on the inverse dielectric function that can characterize the magnetotransport in quantum wires. A brief summary of our findings and some specific remarks are found in Sec. IV.

II. MATHEMATICAL FORMALISM

For a typical Q1DEG in the x-y plane with a parabolic confining potential $V(x)=\frac{1}{2}m^*\omega_0^2x^2$ along the x direction and a magnetic field applied along the z direction in the Landau gauge $[\mathbf{A}=(0,Bx,0)]$ in narrow-gap semiconductors, such as $In_{1-x}Ga_xAs/In_{1-x}Al_xAs$ quantum wire (Fig. 1), the single-particle (of charge $-e$, with $e>0$) Hamiltonian including the

lowest order of the spin-orbit interactions can be expressed as follows:

$$H = H_o + H_r + H_z, \tag{1}$$

where H_o, H_r, and H_z are, respectively, the orbital, Rashba, and Zeeman Hamiltonians defined as follows:

$$H_o = \frac{1}{2m^*}\left(\hat{\mathbf{p}} + \frac{e}{c}\hat{\mathbf{A}}\right)^2 + \frac{1}{2}m^*\omega_0^2 x^2,$$

$$H_r = \frac{\alpha}{\hbar}\left[\hat{\sigma} \times \left(\hat{\mathbf{p}} + \frac{e}{c}\hat{\mathbf{A}}\right)\right]_z,$$

$$H_z = \frac{1}{2}g^*\mu_B B\sigma_z, \tag{2}$$

where α is the Rashba parameter, which describes the strength of the SOI, $\hat{\sigma} \equiv (\sigma_x, \sigma_y, \sigma_z)$ stands for vector of the Pauli spin matrices, $\hat{\mathbf{p}}$ is the momentum operator, g^* is the electron g factor, $\mu_B = e\hbar/(2m_0 c)$ is the Bohr magneton, m_0 is the bare mass of the electron, and the rest of the symbols have their usual meanings. We assume the original two-dimensional electron gas confined in the zero-thickness x-y plane due to a relatively stronger confinement potential $V_c(z)$. The latter is a reasonable approximation for the low charge densities at lower temperatures desired in the experiments on the low-dimensional systems when only the lowest 1D subband (for the z motion) is occupied. This then implies that the z coordinate drops out of the consideration.

A. Eigenfunctions and eigenenergies

The first and foremost thing to compute the excitation spectrum of the charge carriers is to determine the eigenvalues ϵ of the Schrödinger equation $H\psi = \epsilon\psi$, where the eigenfunction $\psi \equiv \psi(\mathbf{r}) \equiv \psi_\uparrow(\mathbf{r})\psi_\downarrow(\mathbf{r})$ is a two-component spinor. Since the Hamiltonian H is translationally invariant in the y direction, the functions $\psi_{\uparrow\downarrow}(\mathbf{r})$ are the plane waves propagating along y axis, i.e., $\psi_{\uparrow\downarrow}(\mathbf{r}) = \exp(ik_y y)\phi_{\uparrow\downarrow}(x)$. Here k_y is the y component of the propagation vector. The equations for $\phi_{\uparrow\downarrow}(x)$ stem from the Schrödinger equation and can be cast, after simple algebraic manipulation, in the form

$$\phi''_{\uparrow\downarrow}(t) + \left[\epsilon_x \mp \gamma\left(\frac{l_0}{l_c}\right)^2 - at^2 - bt\right]\phi_{\uparrow\downarrow}(t) = \left(\frac{l_0}{l_\alpha}\right)\left\{\pm\phi'_{\downarrow\uparrow}(t) + \left[\left(\frac{l_0}{l_c}\right)^2 + k_y l_0\right]\phi_{\downarrow\uparrow}(t)\right\}, \tag{3}$$

where

$$l_0 = \sqrt{\frac{\hbar}{m^*\omega_0}}, \quad l_c = \sqrt{\frac{\hbar}{m^*\omega_c}}, \quad \text{and } l_\alpha = \frac{\hbar^2}{2m^*\alpha} \tag{4}$$

are three length scales involved in the problem and which characterize, respectively, the confinement potential, the magnetic field, and the Rashba SOI. Here ω_0 is the frequency of the harmonic oscillator and $\omega_c = eB/m^*c$ is the cyclotron frequency. The other substitutions are defined as follows:

$$\epsilon_x = (k_x l_0)^2, \quad k_x = \frac{2m^*}{\hbar^2}\epsilon - k_y^2, \quad t = \frac{x}{l_0}, \quad \gamma = \frac{1}{2}g^*\frac{m^*}{m_0}. \tag{5}$$

We observe that as long as the α coupling is finite (i.e., if $l_0/l_\alpha \neq 0$), the coupled equations [Eq. (3)] cannot be solved in an explicitly analytical form. However, in the limit of

$$l_c \ll l_0 \quad \text{and } kl_0 \ll 1 \tag{6}$$

the rotating-wave approximation,[35] which leads to the famous Jaynes-Cummings model (JCM),[36] becomes exact and helps us solve the coupled equations [Eq. (3)] exactly. Clearly, in the aforesaid limits the electrons are strongly localized around the center of the quantum wire and hence remain insensitive to the confining potential. In this limit, there is a crossover to the 2D electron system (2DES) with a perpendicular magnetic field and the Rashba SOI for which the formal identity to the JCM has been asserted.[37] A careful, systematic, and rigorous diagnosis of Eq. (3) enables us to characterize the resultant system with the eigenfunctions $[\uparrow\downarrow \equiv +-]$ (see Appendix)

$$\psi_n^+(k_y) = \frac{1}{\sqrt{L_y A_n}}e^{ik_y y}\begin{pmatrix}\beta_n\phi_{n-1}(x+x_c)\\ \phi_n(x+x_c)\end{pmatrix} \tag{7}$$

and

$$\psi_n^-(k_y) = \frac{1}{\sqrt{L_y A_n}}e^{ik_y y}\begin{pmatrix}\phi_{n-1}(x+x_c)\\ -\beta_n\phi_n(x+x_c)\end{pmatrix}, \tag{8}$$

and the eigenenergies

$$\epsilon^{\pm}_{nk_y} = n\hbar\tilde{\omega} + \epsilon_{k_y} \pm \left[\epsilon_z^2 + \frac{1}{2}nS^2\left(\frac{\alpha}{l_d}\right)^2\right]^{1/2} = n\hbar\tilde{\omega} + \epsilon_{k_y} \pm \frac{1}{2}\hbar\tilde{\omega}\tilde{\epsilon}_n = \left(n \pm \frac{1}{2}\tilde{\epsilon}_n\right)\hbar\tilde{\omega} + \epsilon_{k_y}, \tag{9}$$

where $x_c = k_y(l_d^4/l_c^2)$, $A_n = [1+\beta_n^2]$, $S = [1+(l_d/l_c)^2]$, $\epsilon_{k_y} = \hbar^2 k_y^2/(2m_r)$, $\epsilon_z = \frac{1}{2}\hbar\tilde{\omega}[1-\gamma(l_d/l_c)^2]$, $\tilde{\omega} = \sqrt{\omega_c^2+\omega_0^2}$, $m_r = m^*(\tilde{\omega}^2/\omega_0^2)$, $l_d = \sqrt{\hbar/(m^*\tilde{\omega})}$, $\tilde{\epsilon}_n = \{[1-\gamma(l_d/l_c)^2]^2 + \frac{1}{2}nS^2(l_d/l_\alpha)^2\}^{1/2}$, and $\beta_n = [(\alpha/l_d)\sqrt{nS^2/2}]/\left[\epsilon_z + \sqrt{\epsilon_z^2 + \frac{1}{2}nS^2(\alpha/l_d)^2}\right]$. Here m_r, l_d, x_c, and n are, respectively, the renormalized effective mass, the effective magnetic length, the center of the cyclotron orbit with radius l_d, and the hybrid magnetoelectric subband (HMES) index. Note that the effective magnetic length l_d refers to the typical width of the wave function and reduces to the magnetic length l_c if the confining potential is zero (i.e., if $\omega_0 = 0$). In the limit of a strong magnetic field, the renormalized mass m_r becomes infinite and the system undergoes a crossover to the 2D electron system and hence the Landau degeneracy is recovered. It should be pointed out that a *very-strong-field* limit renders the approximation $\omega_0^2 \ll \omega_c^2$ viable but the essence of the problem is lost. That is why we have purposely retained the terms such as $\tilde{\omega}$, l_d, etc., in order to maintain the *three* length scales in and hence not to lose the charm of the problem. Otherwise, ω_0 will practically vanish from the treatment except for its (explicit) appearance in the renormalized effective mass. In Eqs. (7) and (8), the function $\phi_n(y)$,

with $y=(x+x_c)$, is the Hermite function defined as

$$\phi_n(y) = N_n e^{-y^2/(2l_d^2)} H_n(y/l_d), \tag{10}$$

where L_y is the normalization length and $N_n = 1/\sqrt{\sqrt{\pi} 2^n n! l_d}$ is the standard normalization constant. It seems noteworthy that one can also interpret the third equality of Eq. (9) as if all the (strong) magnetic field has brought to bear is the modification of the zero-point energy of an otherwise Rashba spintronic quantum wire. The modified zero-point energy is thus no longer a constant, but depends upon the magnetic field as well as on the confining potential.

Let us focus on the eigenenergies given by Eq. (9). In Fig. 2, we have plotted the dimensionless energy $\epsilon_n^{\pm}/\hbar\omega_0$ as a function of reduced wave vector $k_y l_0$ (see top and the middle panels) and $\epsilon_n^{\pm}/\hbar\tilde{\omega}$ as a function of the ratio l_0/l_c (see the bottom panel). The top panel represents the situation for the zero magnetic field (i.e., $B=0$) (see Ref. 32). We have chosen the threshold value $l_0/l_\alpha = \sqrt{2}$, where the parabola $\epsilon_\uparrow(n)$ crosses the bottom of parabola $\epsilon_\downarrow(n+1)$. It is easy to verify that for $l_0/l_\alpha < \sqrt{2}$ ($l_0/l_\alpha > \sqrt{2}$) the parabola $\epsilon_\uparrow(n)$ crosses to the right (left) of the bottom of parabola $\epsilon_\downarrow(n+1)$. It is a simple matter to verify that the minimum of the parabola $\epsilon_\downarrow(n+1)$ lies at the point $k_y l_0 = (1/2)(l_0/l_\alpha)$. Applying a (perpendicular) magnetic field is equivalent to enhancing the transverse confining potential on a quantum wire and results in a larger subband separation. One can notice a number of visible effects of nonzero magnetic field (see middle panel): (1) the formerly $k_y=0$ spin degeneracy (cf. top panel) is split, (2) the splitting at $k_y=0$ is a function of the subband index, and (3) the higher the magnetic field, the larger the subband separation and flatter the parabolas at the zone center. In addition, it is observed that the magnetic-field induced splitting can exceed the Zeeman splitting. The bottom panel, where we plot the eigenenergies normalized to the hybrid energy $\hbar\tilde{\omega}$ vs (virtually) the magnetic field, reveals the following: (1) for small magnetic field ($l_0/l_c \leqslant 1$) the energy splitting is almost comparable to the subband separation, (2) for higher subbands SOI-induced splitting leads to anticrossings with neighboring subbands, (3) at higher magnetic field ($l_0/l_c \geqslant 4$) no anticrossings take place, and (4) the splittings may even saturate for large magnetic field. It is noticed that such combined effects of the Rashba SOI and the applied magnetic field on the single electron spectra as described above have some interesting consequences on the collective excitation spectra of the quantum wires (see Sec. III).

It is interesting to note that in the limit of zero SOI (i.e., $\alpha=0$), Eqs. (7) and (8) simplify to

$$\psi_n^{\pm}(k_y) = \frac{1}{\sqrt{L_y}} e^{ik_y y} \phi_n(x+x_c), \tag{11}$$

and Eq. (9) reduces to

$$\epsilon_{nk_y}^{\pm} = \left(n+\tfrac{1}{2}\right)\hbar\tilde{\omega} + \epsilon_{k_y} - \tfrac{1}{2}\gamma\hbar\omega_c. \tag{12}$$

Note that these are virtually the eigenfunction and the eigenenergy for the Q1DEG in the presence of an applied (perpendicular) magnetic field, just as expected. Next, if we look for the ground-state (i.e., $n=0$) eigenfunction and eigenenergy, we obtain exactly Eqs. (11) and (12) with $n=0$. That means that in the lowest hybrid magnetoelectric subband, the Rashba spin splitting does not take place and

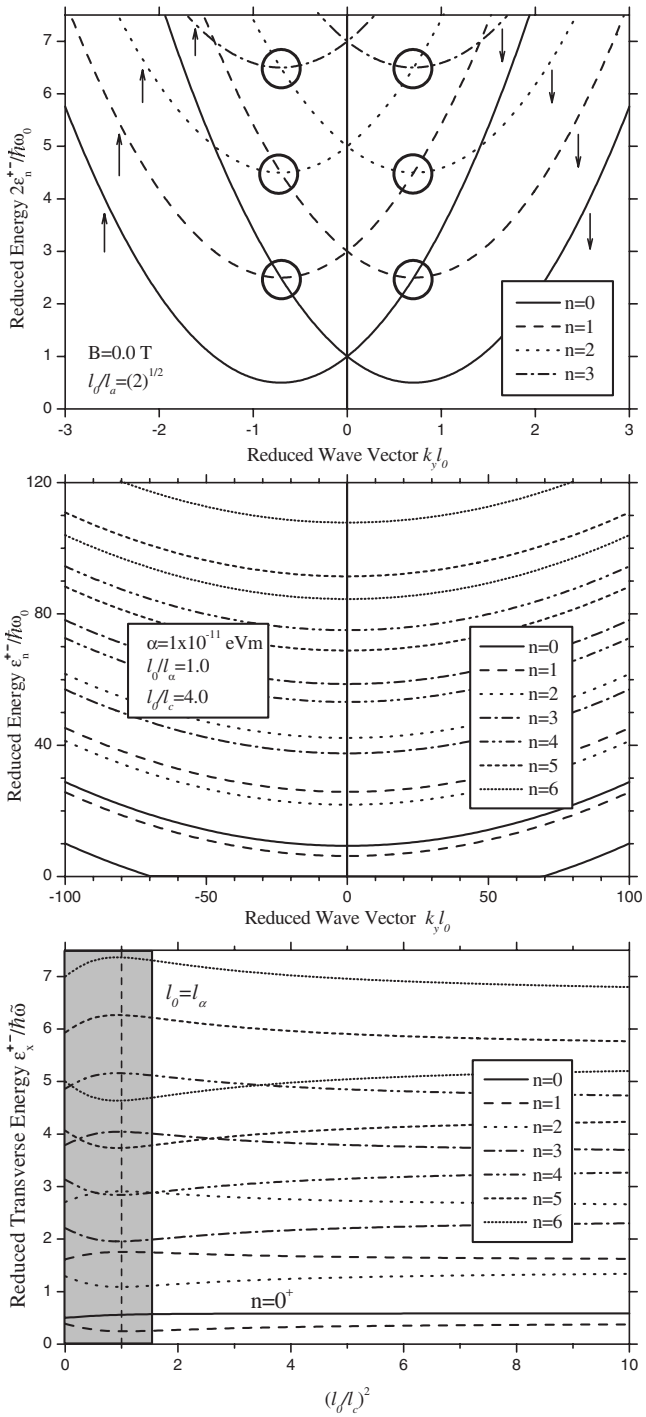

FIG. 2. The dimensionless energy $\epsilon_n^{\pm}/\hbar\omega_0$ vs dimensionless wave vector $k_y l_0$ for $B=0$ (top panel), the same for $B\neq 0$ (middle panel), and the dimensionless transverse energy $\epsilon_n^{\pm}/\hbar\tilde{\omega}$ vs the ratio $(l_0/l_c)^2$ for $B\neq 0$ (bottom panel). The circles in the top panel encircle the bottoms of the parabola $\epsilon_\downarrow(n+1)$. The upper (lower) identical curves in the middle and bottom panels refer to spin-up (spin-down) states. The other parameters are listed inside the picture. The said inequality [in Eq. (6)] does not hold good in the shaded region.

the zero-point energy predominates for $kl_0 \ll 1$ and $\gamma=0$.

B. Nonlocal, dynamic dielectric function

We start with a general expression for the single-particle density-density response function $\chi^0(\cdots)$ given by[1]

$$\chi^0(\mathbf{r},\mathbf{r}';\omega) = \sum_{\zeta\zeta'} \Lambda_{\zeta\zeta'} \psi^*_{\zeta}(\mathbf{r}')\psi_{\zeta'}(\mathbf{r}')\psi^*_{\zeta'}(\mathbf{r})\psi_{\zeta}(\mathbf{r}), \quad (13)$$

where $\mathbf{r} \equiv (x,y)$, $\zeta \equiv \{i,\sigma\}$, with $i \equiv \{k_y,n\}$ and $\sigma \equiv \pm 1$, and the (general) polarizability function $\Lambda_{\zeta\zeta'}$ is defined as

$$\Lambda_{\zeta,\zeta'} \equiv \Lambda^{\sigma\sigma'}_{ij} \equiv \Lambda^{\sigma\sigma'}_{\substack{nk_y \\ n'k'_y}} = \frac{f(\epsilon^{\sigma}_{nk_y}) - f(\epsilon^{\sigma'}_{n'k'_y})}{\epsilon^{\sigma}_{nk_y} - \epsilon^{\sigma'}_{n'k'_y} + \hbar\omega^*}, \quad (14)$$

where $f(x)$ is the well-known Fermi distribution function. $\omega^* = \omega + i\gamma_c$ and small but nonzero γ_c represents the adiabatic switching of the Coulomb interactions in the remote past. For the sake of simplicity, we rewrite Eqs. (7) and (8) symbolically as follows:

$$\psi_{\zeta}(\mathbf{r}) = \phi_{k_y}(y)\phi_{n\sigma}(x+x_c), \quad (15)$$

where

$$\phi_{k_y}(y) = \frac{1}{\sqrt{L_y A_n}} e^{ik_y y} \quad (16)$$

and

$$\phi_{n\sigma}(x+x_c) = \begin{cases} \begin{pmatrix} \beta_n \phi_{n-1}(x+x_c) \\ \phi_n(x+x_c) \end{pmatrix} \equiv \phi^+_n(x+x_c), & \sigma = +1 \\ \begin{pmatrix} \phi_{n-1}(x+x_c) \\ -\beta_n \phi_n(x+x_c) \end{pmatrix} \equiv \phi^-_n(x+x_c), & \sigma = -1. \end{cases} \quad (17)$$

We will revive the original indices later. As such Eq. (13) can be cast in the following form:

$$\chi^0(\mathbf{r},\mathbf{r}';\omega) = \frac{1}{L_y^2} \sum_{k_y k'_y} \sum_{\sigma\sigma'} \sum_{nn'} \Pi^{\sigma\sigma'}_{nn'} e^{iq_y(y'-y)} \phi^*_{n\sigma}(x'+x_c) \times \phi_{n'\sigma'}(x'+x'_c)\phi^*_{n'\sigma'}(x+x'_c)\phi_{n\sigma}(x+x_c), \quad (18)$$

where $x'_c = k'_y l_d^2$, $q_y = k'_y - k_y$ is the 1D momentum transfer, and

$$\Pi^{\sigma\sigma'}_{nn'} = \frac{1}{A_n A_{n'}} \Lambda^{\sigma\sigma'}_{nn'}. \quad (19)$$

Since the translational invariance persists in the y direction, we can Fourier transform this equation with respect to y. For this purpose, we multiply both sides of this equation by $e^{-iq'_y(y'-y)}$ and integrate over y'. The result, after a few straightforward mathematical steps, is

$$\chi^0(x,x';q_y,\omega) = \frac{1}{L_y} \sum_{k_y} \sum_{\sigma\sigma'} \sum_{nn'} \Pi^{\sigma\sigma'}_{nn'} [\phi^*_{n\sigma}(x'+x_c)\phi_{n'\sigma'}(x'+x'_c) \times \phi^*_{n'\sigma'}(x+x'_c)\phi_{n\sigma}(x+x_c)]_{k'_y=k_y+q_y}. \quad (20)$$

Though the specification $k'_y = k_y + q_y$ will be kept in mind, it will be omitted henceforth for the sake of brevity. Next, we recall that the induced particle density, employing Kubo's correlation function, is defined by[1]

$$n_{in}(x;q_y,\omega) = \int dx' \chi^0(x,x';q_y,\omega) V(x';q_y,\omega), \quad (21)$$

where $V = V_{ex} + V_{in}$ is the total potential (energy), with V_{ex} (V_{in}) as the external (induced) potential. The induced potential is further defined by

$$V_{in}(x;q_y,\omega) = \int dx' V_{ee}(x-x';q_y) n_{in}(x';q_y,\omega), \quad (22)$$

where $V_{ee}(\cdots)$ is the Fourier transform of the binary Coulombic interactions and is given by

$$V_{ee}(x-x';q_y) = \frac{2e^2}{\epsilon_b} K_0(q_y|x-x'|), \quad (23)$$

where ϵ_b is the background dielectric constant of the medium in which the Q1DEG is embedded and $K_0(x)$ is the zeroth-order modified Bessel function of the second kind, which diverges as $-\ln(x)$ when $x \to 0$. Equations (21)–(23) together yield

$$V_{in}(x;q_y\omega) = \frac{1}{L_y} \sum_{k_y} \sum_{nn'} \sum_{\sigma\sigma'} \Pi^{\sigma\sigma'}_{nn'} \int dx' V_{ee}(x-x') \times \phi^*_{n'\sigma'}(x'+x'_c)\phi_{n\sigma}(x'+x_c) \int dx'' \times \phi^*_{n\sigma}(x''+x_c)V(x'')\phi_{n'\sigma'}(x''+x'_c). \quad (24)$$

Let us now take the matrix elements of both sides between the states $|m\sigma''>$ and $|m'\sigma'''>$. The result is

$$\langle m\sigma''|V_{in}(x)|m'\sigma'''\rangle = \frac{1}{L_y} \sum_{k_y} \sum_{nn'} \sum_{\sigma\sigma'} \Pi^{\sigma\sigma'}_{nn'} \int dx \int dx' \times \phi^*_{m\sigma''}(x+x_c)\phi_{m'\sigma'''}(x+x'_c)V_{ee}(x-x') \times \phi^*_{n'\sigma'}(x'+x'_c)\phi_{n\sigma}(x'+x_c) \times \langle n\sigma|V(x'')|n'\sigma'\rangle. \quad (25)$$

This equation can be rewritten in a more convenient form as follows:

$$\langle \nu|V_{in}(x)|\nu'\rangle = \frac{1}{L_y} \sum_{k_y} \sum_{\mu\mu'} \Pi_{\mu\mu'} F_{\mu\mu'\nu\nu'}(q_y) \langle \mu|V(x'')|\mu'\rangle, \quad (26)$$

where $\mu \equiv n\sigma$, $\mu' \equiv n'\sigma'$, $\nu \equiv m\sigma''$, and $\nu' \equiv m'\sigma'''$ stand for the composite indices and

$$F_{\mu\mu'\nu\nu'}(q_y) = \int dx \int dx' \phi^*_{n\sigma}(x+x_c)\phi_{n'\sigma'}(x+x'_c) \times V_{ee}(x-x')\phi^*_{m'\sigma'''}(x'+x'_c)\phi_{m\sigma''}(x'+x_c). \tag{27}$$

It is a simple matter to cast Eq. (26) in the following form:

$$\langle \nu|V_{in}(x)|\nu'\rangle = \sum_{\mu\mu'}\left[\delta_{\mu\nu}\delta_{\mu'\nu'} - \frac{1}{L_y}\sum_{k_y}\Pi_{\mu\mu'}F_{\mu\mu'\nu\nu'}(q_y)\right] \times \langle \mu|V(x'')|\mu'\rangle. \tag{28}$$

Now, since V_{ex} and V are related through

$$V_{ex}(x) = \int dx' \epsilon(x,x')V(x'), \tag{29}$$

we can deduce from Eq. (28) the elements of the nonlocal, dynamic dielectric function expressed as follows:

$$\epsilon_{\mu\mu'\nu\nu'} = \delta_{\mu\nu}\delta_{\mu'\nu'} - \frac{1}{L_y}\sum_{k_y}\Pi_{\mu\mu'}F_{\mu\mu'\nu\nu'}(q_y). \tag{30}$$

It would be helpful to rewrite the function $F_{\mu\mu'\nu\nu'}$ in Eq. (27) in the following form:

$$F_{\mu\mu'\nu\nu'}(q_y) \equiv N^{\sigma\sigma'\sigma''\sigma'''}_{nn'mm'} = \int dx \int dx' V_{ee}(x-x')M^{\sigma\sigma'\sigma''\sigma'''}_{nn'mm'}, \tag{31}$$

where

$$M^{\sigma\sigma'\sigma''\sigma'''}_{nn'mm'} = \phi^*_{n\sigma}(x+x_c)\phi_{n'\sigma'}(x+x'_c)\phi^*_{m'\sigma'''}(x'+x'_c)\phi_{m\sigma''}(x'+x_c). \tag{32}$$

Equation (30) can be easily cast in the following form:

$$\tilde{\epsilon}(q_y,\omega) = \begin{bmatrix} \delta - A^{++}_{nn'}N^{++++}_{nn'mm'} & -A^{++}_{nn'}N^{+++-}_{nn'mm'} & -A^{++}_{nn'}N^{++-+}_{nn'mm'} & -A^{++}_{nn'}N^{++--}_{nn'mm'} \\ -A^{+-}_{nn'}N^{+-++}_{nn'mm'} & \delta - A^{+-}_{nn'}N^{+-+-}_{nn'mm'} & -A^{+-}_{nn'}N^{+--+}_{nn'mm'} & -A^{+-}_{nn'}N^{+---}_{nn'mm'} \\ -A^{-+}_{nn'}N^{-+++}_{nn'mm'} & -A^{-+}_{nn'}N^{-++-}_{nn'mm'} & \delta - A^{-+}_{nn'}N^{-+-+}_{nn'mm'} & -A^{-+}_{nn'}N^{-+--}_{nn'mm'} \\ -A^{--}_{nn'}N^{--++}_{nn'mm'} & -A^{--}_{nn'}N^{--+-}_{nn'mm'} & -A^{--}_{nn'}N^{---+}_{nn'mm'} & \delta - A^{--}_{nn'}N^{----}_{nn'mm'} \end{bmatrix}, \tag{33}$$

where $A^{\sigma\sigma'}_{nn'} = (1/L_y)\Sigma_{k_y}\Pi^{\sigma\sigma'}_{nn'}$ and δ stands for $\delta = \delta_{nm}\delta_{n'm'}$ for the sake of brevity. Notice that until now we have invoked no approximation whatsoever with respect to the number of the HMESs n involved in the problem. As such, Eq. (33) represents the generalized nonlocal, dynamic dielectric function for a realistic quantum wire in the presence of a perpendicular magnetic field and the Rashba SOI. In that sense, every block of the matrix in Eq. (33) is, in general, an $\infty \times \infty$ matrix.

C. On the symmetry of the confining potential and on limiting the hybrid magnetoelectric subband

In the absence of any applied magnetic field, it is well known by now[1] that for a symmetric potential, $V_{ijkl}(q_y)$ (i.e., the matrix elements of the Fourier transformed Coulombic interaction) is strictly zero for an arbitrary value of the propagation vector q_y provided that the sum $i+j+k+l$ is an odd number. This is because the wave function is either symmetric or antisymmetric under space reflection. However, in the presence of an applied (perpendicular) magnetic field the situation takes a different turn. In the latter case, even though the confining potential is symmetric and the sum $i+j+k+l$ is an odd number, $V_{ijkl}(q_y)$ is *not* strictly zero. This can, in the first instance, be attributed to the fact that in the presence of an applied magnetic field (in the Landau gauge), the center of the cyclotron orbit is displaced from zero by a finite distance (in the present case x_c). This in turn leads to an (imposed) anisotropy in the system causing, for instance, the scalar dielectric function to become a dielectric tensor (with off-diagonal elements being nonzero). The same anisotropy is also known to be (implicitly) responsible for lifting the intrinsic degeneracy of the quantum states of an isolated system by subjecting the system to an external force which is spherically *asymmetric*. For a system of charged particles, the forces arising from an applied magnetic field are of this nature and provide a means for the complete removal of the degeneracy. These are some of the fundamental reasons why the study of magnetic-field effects, particularly in the low-dimensional systems, has drawn so much attention in the past two decades.[1] The remarks made on $V_{ijkl}(q_y)$ only help us understand the coupling and/or decoupling of, e.g., the intrasubband and intersubband plasmons (see, e.g., Ref. 32) and have nothing to do with the many-body effects.

To make sure how the symmetry arguments (as stated above) work on the quantity V_{ijkl} (with $i+j+k+l$ as the odd number) in case of an applied magnetic field, we computed carefully the integrals for V_{0010}, V_{0021}, V_{1110}, and V_{1121} independently using FORTRAN and MATHEMATICA. The results up to eighth place of the decimal are as follows: (1) For $y_0=0$ (i.e., when $B=0$), we find that $V_{0010}=V_{0021}=V_{1110}=V_{1121}=0$ for any value of $q_y l_d$ and (2) for $y_0=0.0001$ (i.e., when $B \neq 0$), we obtained $V_{0010}=0.000\,483\,63$, $V_{0021}=0.000\,831\,38$,

$V_{1110}=0.000\,173\,88$, and $V_{1121}=0.000\,354\,37$ for $q_y l_d=0.5$. After spending considerable amount of time on verifying how the integrals V_{ijkl} (with $B\neq 0$ and $i+j+k+l=$odd number) behave, we came to the conclusion that as long as $y_0 \to 0$, one can safely apply the situation for the zero magnetic field. In case of a strong magnetic field (as is the case here), one has no other option but to retain and compute all the integrals, both with $i+j+k+l=$ odd and even, because none will strictly vanish for an arbitrary value of the propagation vector.

In the realistic samples the experiments are generally performed on an array of quantum wires in order to obtain measurable signal strength. However, because the Coulomb coupling between the neighboring wires (in the state-of-the-art high quality multiwire systems) is very weak, one is allowed to interpret the experiments dominantly in terms of excitations in an isolated quantum wire. Although most of the samples in the experiments performed to date (on, e.g., $GaAs/Ga_{1-x}Al_xAs$ systems) had multiple subbands occupied,[11–16] theoretically it is very difficult to compute the excitation spectrum for a multiple-subband model. This is because the generalized dielectric function matrix is bound to have the dimensions of $N^2\times N^2$, where N is the number of subbands in the model. The situation is even more complicated for the case where the Rashba SOI is considered in the quantum wires made up of narrow-gap InAs systems (as is the case here). For this reason, we decide to keep the complexity to a minimum and limit ourselves to a two-subband model, with only the lowest one occupied (i.e., $n,n',m,m' \equiv 1,2$). In this case, our generalized dielectric function becomes a 16×16 matrix. Since the second subband is assumed to be unoccupied, we have $A_{22}^{\sigma\sigma'}=0$. This means that $\tilde{\epsilon}(q_y,\omega)$ is finally a 12×12 matrix to be dealt with at the computational level. That implies that there are 36 different types of integrals which will finally define the quantities $N_{nn'mm'}^{\sigma\sigma'\sigma''\sigma'''}$ in the 12×12 matrix generated from Eq. (33).

D. Density of states, Fermi energy, magnetic depopulation, and hybrid magnetoelectric subband

Analytical diagnosis requires that we start with Eq. (9)—particularly its third equality. We can write the Fermi momentum in spin-up and spin-down channels as follows:

$$k_F^+ = \frac{1}{\hbar}[2m_r(\epsilon-\epsilon_n^+)]^{1/2} \tag{34}$$

and

$$k_F^- = \frac{1}{\hbar}[2m_r(\epsilon-\epsilon_n^-)]^{1/2}, \tag{35}$$

where $\epsilon_n^{\pm}=(n\mp\tilde{\epsilon}_n/2)\hbar\tilde{\omega}$. These equations can be used to obtain a simple relation between the Fermi momenta of the two channels. This is given by $(k_F^+)^2-(k_F^-)^2=k_\alpha^2$, where $k_\alpha=\sqrt{(2m_r/\hbar^2)\tilde{\epsilon}_n\hbar\tilde{\omega}}$ is termed as effective Rashba momentum. Imposing the condition of electron number conservation;

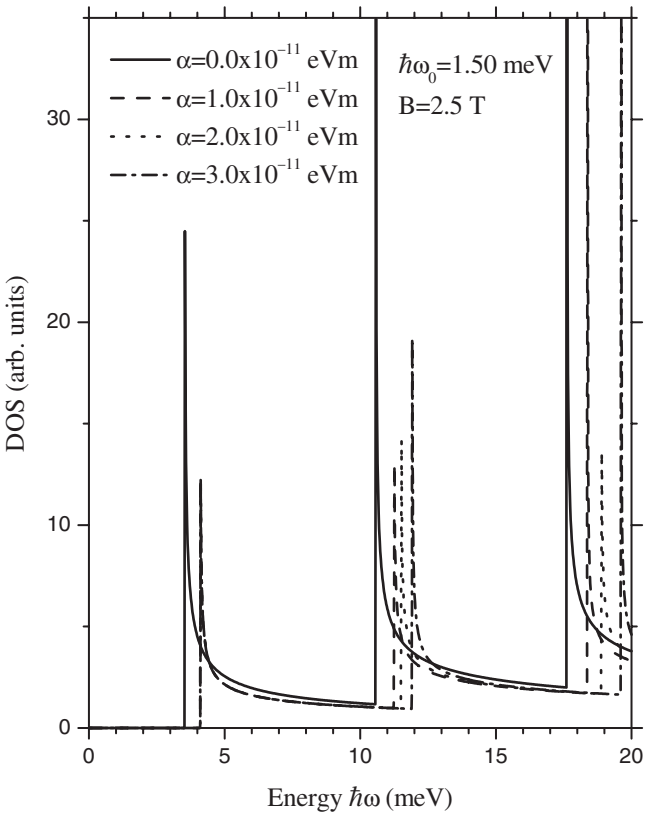

FIG. 3. The density of states for a quasi-1DEG with the subband spacing $\hbar\omega_0=1.5$ meV and the magnetic field $B=2.5$ T. The solid, dashed, dotted, and dash-dotted curves correspond, respectively, to $\alpha=0.0$, 1.0×10^{-11}, 2.0×10^{-11}, and 3.0×10^{-11} eV m. The other parameters are listed inside the picture. We call attention to the lowest peak for nonzero α.

$$n_{1D}=n_{1D}^+ + n_{1D}^- = \frac{1}{\pi}k_F^+ + \frac{1}{\pi}k_F^-, \tag{36}$$

we obtain the corresponding n-dependent 1D density of states (DOS) per unit length expressed as

$$g_n^{1D}(\epsilon) = \frac{1}{2\pi}\left(\frac{2m_r}{\hbar^2}\right)^{1/2} \times[(\epsilon-\epsilon_n^+)^{-1/2}\theta(\epsilon-\epsilon_n^+)+(\epsilon-\epsilon_n^-)^{-1/2}\theta(\epsilon-\epsilon_n^-)]. \tag{37}$$

Hence the total density of states per unit length is the quasi-1D expression given by

$$g_{Q1D}(\epsilon)=\sum_n g_n^{1D}(\epsilon). \tag{38}$$

The total density of states for various values of the Rashba parameter α, neglecting the lifetime broadening, is depicted in Fig. 3. It is interesting to note that the consecutive peaks of DOS are seen to be equidistant in energy by an amount of $\hbar\tilde{\omega}$ for $\alpha=0$, just as expected. However, the separation between DOS peaks increases with increasing α, even though the rule of equidistance is still valid. This is simply because the factor modifying the zero-point energy $\tilde{\epsilon}_n$ increases with

increasing α. The lowest peak for nonzero α lies at the same position ($\hbar\omega$=4.11 meV) for all three values. This is not surprising. For the lower energy only the n=0 counts in order to satisfy the Heaviside step function. That means that the first peak lies at $\hbar\omega=\epsilon_z$. It has also been observed that the number of peaks decreases with increasing magnetic field.[1] The number of occupied subbands and the position of the Fermi level follow from

$$n_{1D}(\epsilon) = \frac{1}{\pi}\left(\frac{2m_r}{\hbar}\right)^{1/2}\sum_n \times[(\epsilon_F-\epsilon_n^+)^{1/2}\theta(\epsilon_F-\epsilon_n^+)+(\epsilon_F-\epsilon_n^-)^{1/2}\theta(\epsilon_F-\epsilon_n^-)] = \sum_n N_n^{1D}, \tag{39}$$

where n_{1D} is the number of electrons per unit length and N_n^{1D} stands for the subband population. It is a simple matter to reproduce the zero-SOI results from Eqs. (37)–(39). In the limit of a strong magnetic field—as is the case here—the subband separation $\Delta\epsilon$ increases and the electrons appear heavier leading to a flattening of the subband dispersion. Then the magnetic confinement dominates over the electrostatic one and the initial parabolic subband dispersions gradually turn into dispersionless Landau levels as in the 2D case because the kinetic energy is practically quenched. Both of these effects can easily be seen by plotting the Landau fan using, e.g., Eq. (9), with or without the Rashba SOI. Figure 4 plotted for α=0 clearly demonstrates the validity of these remarks. Because of this diamagnetic shift, a successive magnetic depopulation of the subbands occurs and oscillations akin to Shubnikov–de Haas oscillations take place in magnetoresistance.[11] When a particular HMES is just depopulated, we have $\epsilon_F=\epsilon_n^{\pm}$. Hence we get the following from Eq. (39):

$$n_{1D} = \frac{1}{\pi}\sqrt{2m_r/\hbar^2}\sum_{n'}[(\epsilon_F-\epsilon_{n'}^+)^{1/2}+(\epsilon_F-\epsilon_{n'}^-)^{1/2}] = \frac{2}{\pi}\sqrt{2m_r/\hbar}\sqrt{\tilde{\omega}}\sum_{n'}(n-n')^{1/2} = \frac{2}{\pi}\sqrt{2m_r/\hbar}\sqrt{\tilde{\omega}}\sum_{\nu}^{n}(\nu)^{1/2}. \tag{40}$$

If we replace the summation by an integration, we obtain

$$n_{1D} = \frac{4}{3\pi}\sqrt{2m_r/\hbar}\sqrt{\tilde{\omega}}n^{3/2}. \tag{41}$$

For strong magnetic fields (lower values of n), Eq. (41) yields the following:

$$n \approx \frac{1}{\omega_c}\left[\frac{3\pi}{4}n_{1D}\omega_0\left(\frac{\hbar}{2m^*}\right)^{1/2}\right]^{2/3}. \tag{42}$$

Equations (40)–(42) clearly substantiate that the hybrid magnetoelectric subband index n is independent of the Rashba parameter α and hence of the spin-orbit interaction, just as expected intuitively. The slope of Eq. (42) does not give the carrier concentration as simply as in the 2D case. In the opposite limit of weak magnetic fields (higher values of n), Eqs. (40) and (41) show a pronounced departure from linearity in n vs B^{-1} as is usually observed in experiments. The general behavior of $n(B^{-1})$ is illustrated in Fig. 5 for the set of parameters listed in the figure.

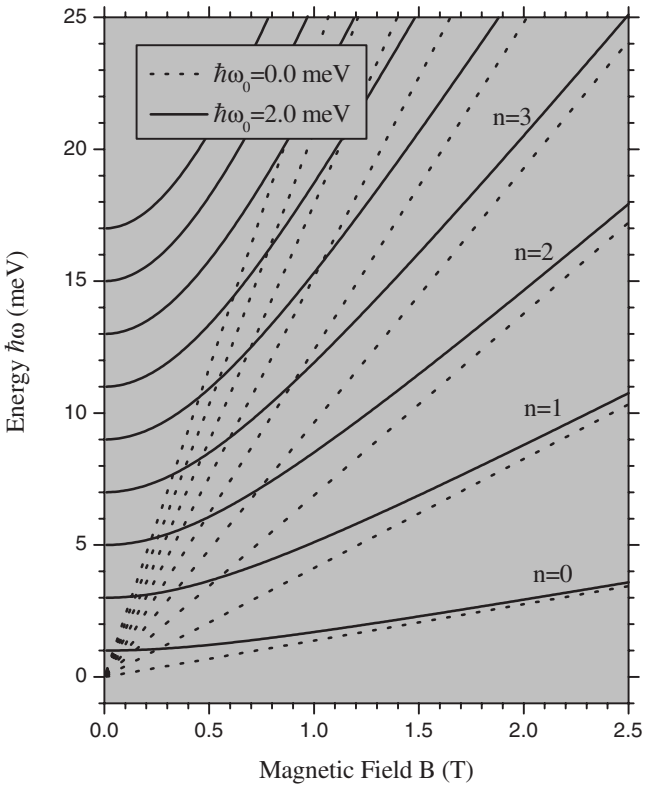

FIG. 4. The nonlinear fan diagram for the quasi-1DEG. The dotted lines show several 2D Landau levels and the solid lines are for the hybrid magnetoelectric confinement potential. Here n refers to the number of the HMES. The parameters are the same as listed in the text.

The self-consistent solutions of Eq. (39) for the Fermi energy and the subband population vs magnetic field are plotted in Fig. 6. The top panel refers to the case of zero SOI (i.e., α=0) and indicates that there are seven occupied subbands just before the magnetic field is switched on. It shows how these subbands are magnetically depopulated. The peaks in the Fermi energy occur when there is a depopulation of the 1D subband and the number of peaks is consistent with the number of initially occupied subbands. The middle panel, in the presence of Rashba SOI ($\alpha\neq 0$), shows how the spin-up states can saturate and the spin-down states continue to successively depopulate with the magnetic field. The bottom panel shows the resultant Fermi energy and the subband depopulation accounting for both the spin-up and spin-down states. The results in the bottom panel demonstrate that the two spin channels together would not allow a complete magnetic depopulation of the subbands.

E. Dielectric function in the special limit of α=0

In the special limit of no spin-orbit interaction, Eq. (33) for a two-subband model simplifies to the following form:

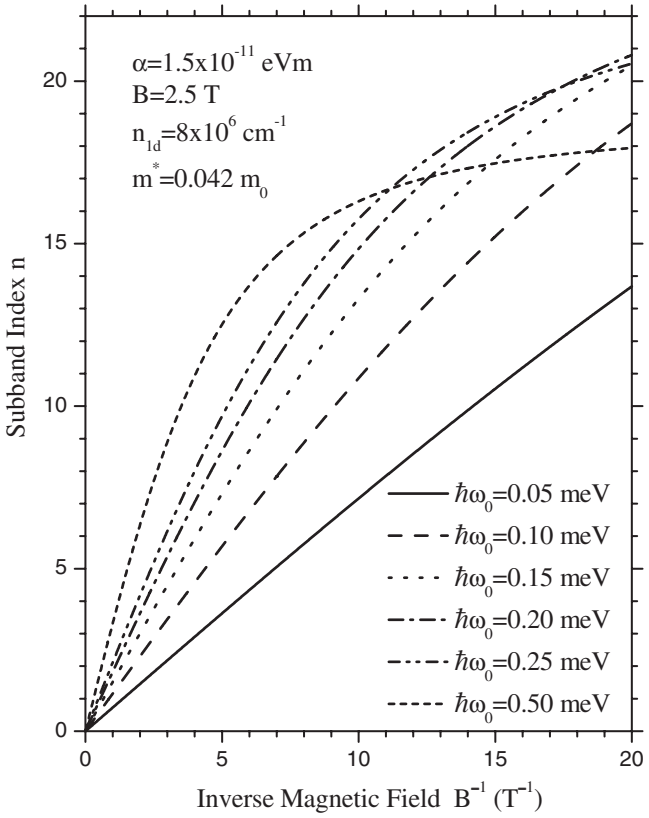

FIG. 5. The subband index n vs inverse magnetic field B^{-1} for harmonic potential. The 1D charge density is held constant ($n_{1D}=8\times10^6$ cm^{-1}), while the strength of the confinement is varied by means of the characteristic energy $\hbar\omega_0$. The parameters are listed inside the picture.

$$\tilde{\epsilon}(q_y,\omega)=\begin{bmatrix} 1-A_{11}N_{1111} & -A_{11}N_{1112} & -A_{11}N_{1121} \\ -A_{12}N_{1211} & 1-A_{12}N_{1212} & -A_{12}N_{1221} \\ -A_{21}N_{2111} & -A_{21}N_{2112} & 1-A_{21}N_{2121} \end{bmatrix}. \tag{43}$$

The determinant of the matrix in Eq. (43) equated to zero furnishes the collective excitation spectrum of magnetoplasmons for a quantum wire in the presence of a harmonic confining potential and an applied (perpendicular) magnetic field within a two-subband model. We still need to clarify an important issue here. We have seen above that the Rashba SOI does not affect at all the dynamics of the resultant system in the ground (HMES) state (i.e., $n=0$), except for the fact that the Zeeman energy should leave its impression. In addition, certain eigenfunctions [in Eqs. (7) and (8)] cannot behave properly for taking $n=0$ and may well remain undefined. Therefore, one has to have $n=1$ ($n=2$) for the ground state (first excited state) in the presence of Rashba SOI and the magnetic field. However, neglecting the SOI but keeping the magnetic field legitimately removes such physical constraint on the system and we can safely take $n=0$ ($n=1$) for the lowest (first excited) subband state. This then implies that we still need to conform Eq. (43) such that the subscript $1\rightarrow0$ and $2\rightarrow1$ for all practical purposes.

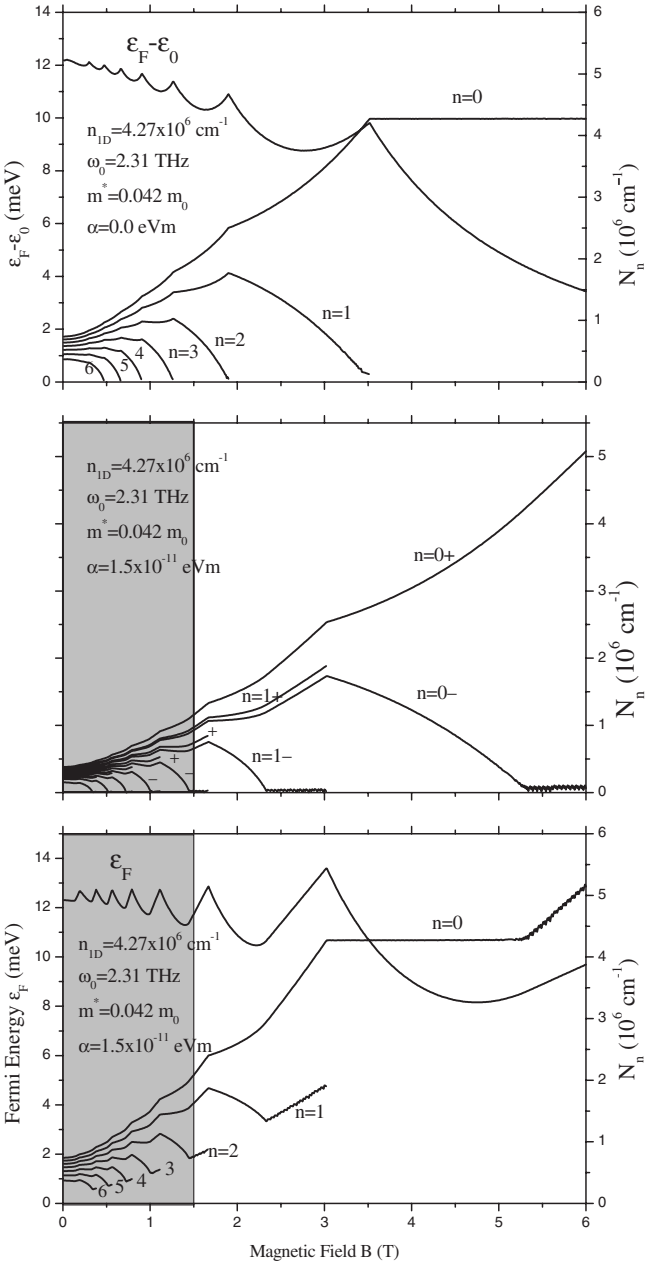

FIG. 6. The variation of the Fermi energy ϵ_F and the subband occupations N_n^{1D} with magnetic field. The Rashba SOI is excluded in the top panel and included in the middle and bottom panels. The middle panel shows the subband occupations for the spin-up and spin-down states separately. The bottom panel gives the resultant picture for the two spin channels considered together. The parameters are listed inside the picture. The said inequality fails to hold good in the shaded region.

F. Remarks on the limitations of earlier perturbative approaches

Ever since its inception in the 1950s, the random-phase approximation (RPA) has known no bounds as regards its applicability for studying the collective as well as single-particle excitation spectra of diverse kinds of systems—with or without including the thermal, electric, magnetic, and/or

many-body effects. Although RPA was envisioned and polished as a high-density approximation, it has been used with remarkable success in the low-dimensional systems as well where the charge densities are only moderate. This is attributed to the fact that the effective coupling constant $r_s = r_0/a_0$ (where r_0 is the mean distance between electrons and a_0 is the effective Bohr radius) is small for low-effective-mass systems since a_0 is inversely proportional to the effective mass. (In $In_{1-x}Ga_xAs$, $m^* = 0.042m_0$.)

Li and Das Sarma[18] studied the magnetoplasmons in quantum wires within the RPA. They stated that since the eigenfunction [see, e.g., Eq. (11)] in the x direction depends on the k_y (in the Landau gauge), this reflects a gauge-independent fact that x and y directions are coupled in the presence of a perpendicular magnetic field and that this causes some difficulties in calculating the excitation spectrum. In order to avoid the apparent difficulty they expanded the eigenfunction in Taylor series and unnecessarily complicated the situation. The result was that they could never observe such interesting features as the existence of intersubband magnetoplasmon that resembles the magnetoroton later predicted in Ref. 19. Wendler and Grigoryan,[20] who pursued a scheme similar to that in Ref. 18, also happened to miss the magnetoroton mode even though it was then already predicted.[19] The fact of the matter is that the term x_c, which simply dictates that the presence of the magnetic field has shifted the center of the orbit from zero to x_c, causes no difficulty whatsoever.

In this subsection, we only aim to demonstrate the dependence of the coefficient of k_y (in x_c) on the magnetic field. This is done in Fig. 7, which shows that this dimensionless parameter λ $[=l_d^4/(l_c^2 l_0^2)]$ is, in fact, small in both weak- and strong-field limits. In the weak-field limit it depends on B linearly while in the strong-field limit it goes to zero as $1/B$. It is simple to ascertain that δ attains its maximum at $\omega_c = \omega_0$. As such, x_c can always be regarded as a small quantity. However, this does not justify an unnecessary expansion of $\phi_n(x+x_c)$ as it was done in Refs. 18 and 20. Next, we plot in Fig. 8 the magnetic field dependence of the factor $\tilde{\epsilon}_n$ that modifies the zero-point energy for the two spin states and about which all the fuss is made. It is not difficult to verify that the maximum of $\tilde{\epsilon}_n$ lies at the magnetic field B that satisfies the following equality:

$$P(\tilde{\omega} + \omega_c)\left[1 - \frac{1}{2}\frac{\omega_c(\tilde{\omega} + \omega_c)}{\omega_0^2}\right] - \gamma(\tilde{\omega} - \gamma\omega_c) = 0, \quad (44)$$

where $P=(n/2)(l_d^2/l_\alpha^2)$. It is observed that all finite-n curves at very high magnetic field become asymptotic to $\tilde{\epsilon}_n = 1.168$, which is exactly the value of $\tilde{\epsilon}_n$ for $n=0$ for a strong B.

Before we close this section, it is noteworthy that after obtaining the solutions [Eqs. (7)–(9)] of the otherwise coupled equations [Eq. (3)]—within the strong-field limit—the whole formalism is an exact standard RPA. Does this mean that we are obliged to feed the parameters which strictly obey the inequality $l_c \ll l_0$? The answer, in principle, is yes. However, we found, after countless *hit and trial* that we loose nothing and still retain essential physics and charm of the problem if we feed the parameters which only moderately satisfy the above inequality.

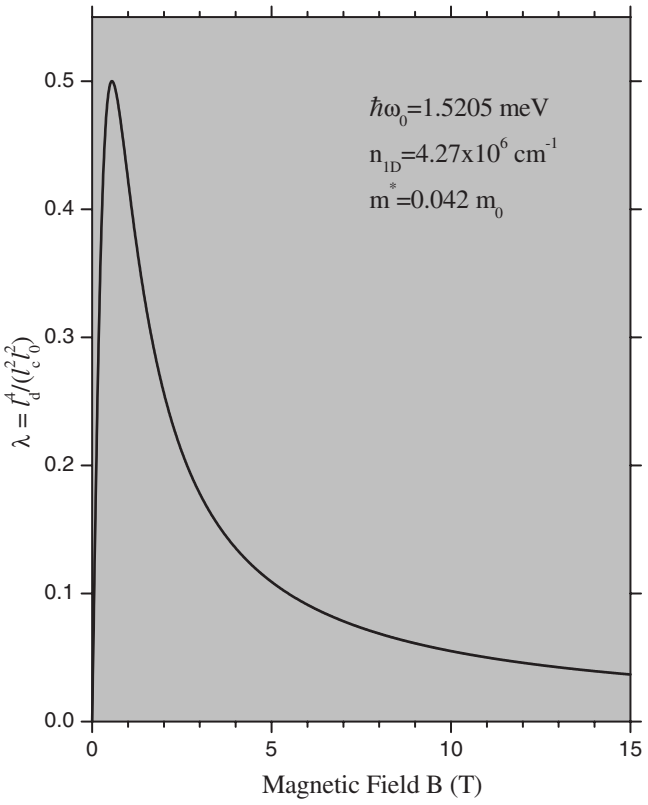

FIG. 7. The normalized coefficient λ (of k_y in the term x_c that defines the center of cyclotron orbit) as a function of the magnetic field B. The parameters are listed inside the picture.

III. ILLUSTRATIVE EXAMPLES ON MAGNETOPLASMON EXCITATIONS

This section is devoted to discuss our illustrative numerical examples on the magnetoplasmon excitations in a Q1DEG within a two-subband model in the presence of a perpendicular magnetic field B and the Rashba spin-orbit interactions, computed at $T=0$ K. We do so by examining the influence of several parameters involved in the analytical results. These are, for instance, the Rashba parameter α, the 1D charge density n_{1D}, and the magnetic field B. The material parameters used are effective mass $m^* = 0.042m_0$, electron g-factor $g=-8.0$, Bohr magneton $\mu_B = 0.9273 \times 10^{-20}$ erg/G, background dielectric constant $\epsilon_b = 13.9$, Rashba parameter $\alpha = 1.5 \times 10^{-11}$ eV m, 1D charge density $n_{1D} = 1.0 \times 10^6$ cm^{-1}, and the effective confinement width of the harmonic potential well, estimated from the extent of the Hermite function, $w_{eff} = 40.19$ nm, as appropriate for the *narrow* channels of the $In_{1-x}Ga_xAs$ system until and unless stated otherwise. Notice that the Fermi energy ϵ_F varies in the case where the charge density n_{1D} or the magnetic field B is varied. For the sake of comparison, we will also present the numerical results without the Rashba SOI (i.e., with $\alpha = 0$).

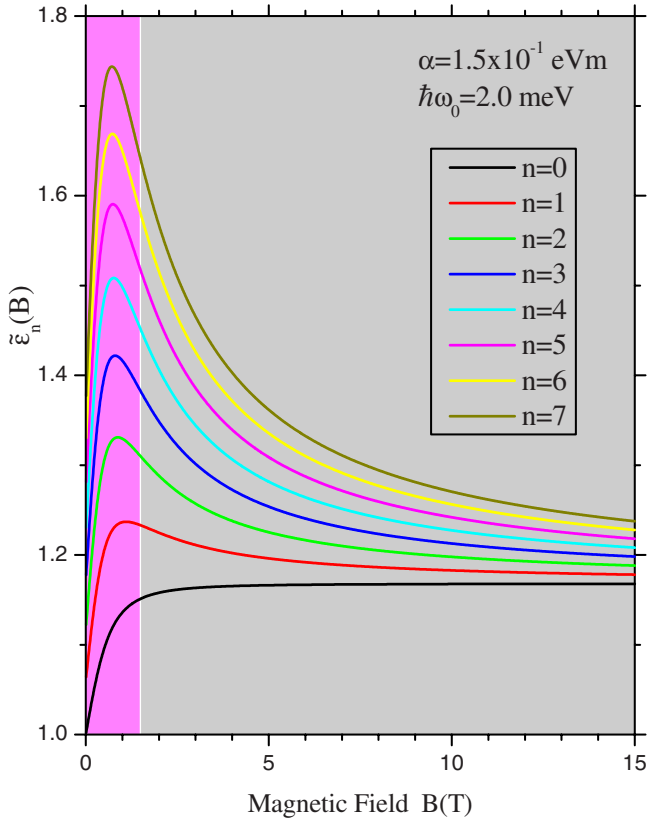

FIG. 8. (Color online) The factor $\tilde{\epsilon}_n$ as a function of the magnetic field B. The parameters are listed inside the picture. The maximum for every curve is exactly the value of B that satisfies Eq. (44). The said inequality does not hold good in the shaded (pink) region.

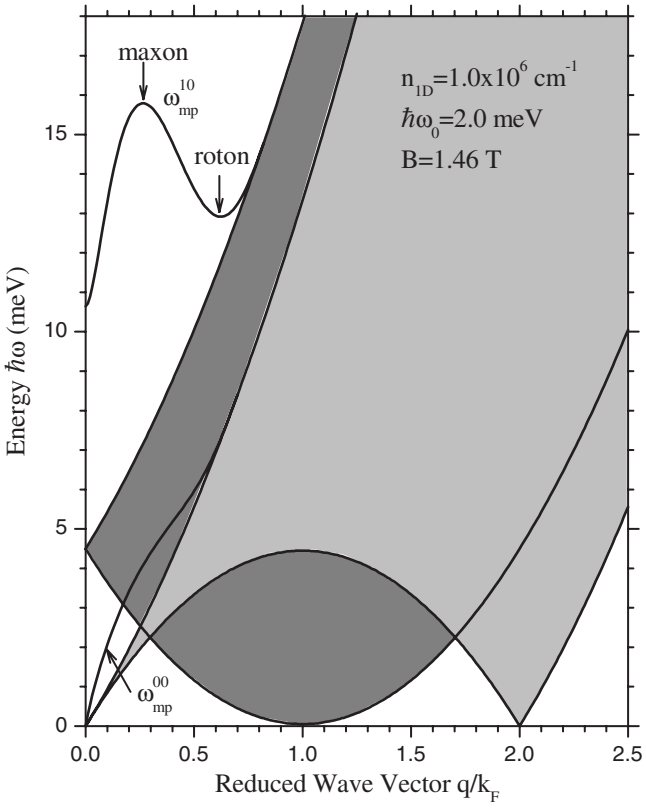

FIG. 9. Magnetoplasmon dispersion plotted as energy $\hbar\omega$ vs reduced wave vector q/k_F, for the given values of n_{1D}, $\hbar\omega_0$, and B. Here we take $\alpha=0$ in order to exclude the Rashba SOI. The light (dark) shaded region refers, respectively, to the intrasubband (intersubband) SPE. The bold solid curve marked as ω_{mp}^{00} (ω_{mp}^{10}) is the intrasubband (intersubband) CME. The parameters are as given inside the picture.

A. Magnetoplasmon dispersion without spin-orbit interaction (i.e., $\alpha=0$)

Figure 9 illustrates the magnetoplasmon dispersion for the Q1DEG without the Rashba spin-orbit interaction, for the given values of n_{1D}, $\hbar\omega_0$, and B. This light (dark) shaded region refers, respectively, to the intrasubband (intersubband) single-particle excitation (SPE). The bold solid curve marked as ω_{mp}^{00} (ω_{mp}^{10}) is the intrasubband (intersubband) collective (magnetoplasmon) excitation (CME). The intrasubband CME starts from the origin and merges with the upper edge of the intrasubband SPE at ($q_y/k_F=0.65$, $\hbar\omega=7.67$ meV) and thereafter ceases to exist as a bonafide, long-lived CME. The intersubband CME starts at ($q_y/k_f=0$, $\hbar\omega=10.64$ meV), attains a maximum at ($q_y/k_f=0.27$, $\hbar\omega=15.79$ meV), reaches its minimum at ($q_y/k_f=0.62$, $\hbar\omega=12.92$ meV), and then rises up to merge with the upper edge of the intersubband SPE at ($q_y/k_f=0.81$, $\hbar\omega=14.62$ meV). The most interesting aspect of this excitation spectrum is the existence of this intersubband CME (henceforth referred to as the magnetoroton). Notice that the magnetoroton (MR) changes its group velocity twice before merging with the respective SPE. The magnetized Q1DEG (or the *realistic* quantum wire system) has this unique characteristic of supporting the MR; no other low-dimensional system is, to the best of our knowledge, known to possess this ability. The interesting thing about its very occurrence leads us to infer that you do not have to *overplay* with the theory, as was done in Refs. 18 and 20. It is a simple matter to check (analytically) why the energy of the lower branch of the intrasubband SPE goes to zero at $q_y=2k_F$, why the lower branch of the intersubband SPE observes its *minimum* (*not zero*) at $q_y=k_F$, and why the intersubband SPE starts at the subband spacing ($\hbar\tilde{\omega}=4.4915$ meV) at the origin. At $q_y=0$, the energy difference between the intersubband CME and SPE is a manifestation of the many-body effects such as depolarization and excitonic shifts.[1]

Figure 10 depicts the evolution of the magnetoroton and the upper edge of the intersubband SPE with the intensity of the magnetic field B. Notice that at very low field ($B\leqslant 0.5$ T) it is hardly expected that the usual intersubband magnetoplasmon will turn into a rotonlike mode. However, as the field intensity grows (e.g., at $B\geqslant 1.0$ T) the intersubband magnetoplasmon starts showing some signs of turning into a magnetoroton. At $B=1.5$ T, this mode has already attained a full form of a magnetoroton mode. It is also noticeable that at much higher magnetic field the sharp roton minimum starts softening, even though it maximum is still relatively well defined. The excitations associated with momenta close to the MR's linear region, its maximum, and its minimum are sometimes called phonons, maxons, and ro-

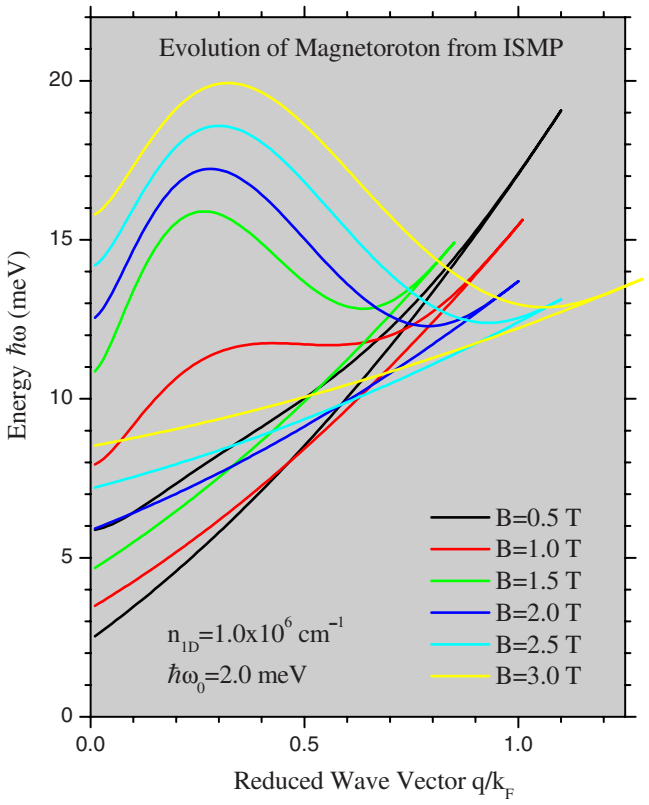

FIG. 10. (Color online) The evolution of the magnetoroton alongside the upper edge of the intersubband SPE (corresponding, for example, to Fig. 9) as a function of the reduced wave vector q/k_F, for the given values of B. Again, we take $\alpha=0$ in order to neglect the Rashba SOI. The other parameters are listed inside the picture.

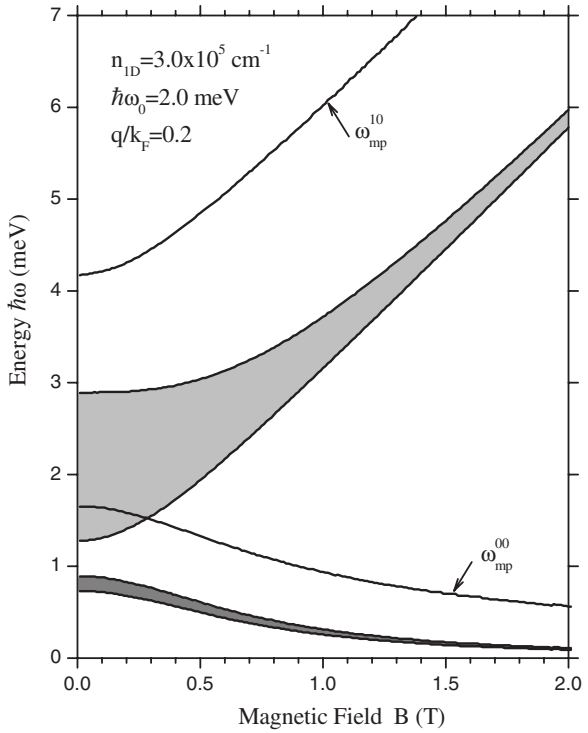

FIG. 11. Magnetoplasmon dispersion plotted as energy $\hbar\omega$ vs magnetic field B, for the given values of n_{1D}, $\hbar\omega_0$, and q_y/k_F. We take $\alpha=0$ in order to neglect the Rashba SOI. The light (dark) shaded region refers, respectively, to the intersubband (intrasubband) SPE. The bold solid curve marked as ω^{00}_{mp} (ω^{10}_{mp}) is the intrasubband (intersubband) CME. The parameters are given inside the picture.

tons, respectively. It is worth mentioning that roton features are among the most significant manifestations of the particle-particle interactions. They arise from the interplay between direct and exchange terms of the electron gas and the depth of the minimum is determined by the strength of the exchange vertex corrections. For the rest, the figure speaks itself so well that we do not need to describe it.

Figure 11 shows the magnetoplasmon dispersion as a function of the magnetic field for the realistic quantum wire, for a given value of the wave vector. The light (dark) shaded region refers, respectively, to the intersubband (intrasubband) SPE. The bold solid curve marked as ω^{00}_{mp} (ω^{10}_{mp}) is the intrasubband (intersubband) CME. Note that the intrasubband magnetoplasmon emerges from inside the intersubband single-particle continuum. It should not be considered as an inherent characteristic of the Rashba spintronic Q1DEG, rather simply a result of the choice of our set of parameters. For other values of the wave vector, this magnetoplasmon can start from even higher energy inside the intersubband SPE or even entirely below this upper SPE having some energy gap below the intersubband SPE. The most prominent feature of this spectrum is the negative-B dispersion of the intrasubband magnetoplasmon, which is a unique behavior observed so far for the edge plasmons and magnetoplasmons whose frequencies are determined by the circumference of the (finite-size) samples. The slope of this negative-B dispersion depends on the density profile as well as on the wire width. The intersubband magnetoplasmons exhibit a positive-B dispersion.

Figure 12 displays the magnetoplasmon dispersion as a function of the 1D charge density n_{1D} for the realistic quantum wire, for the given values of $\hbar\omega_0$, B, and q_y/k_F. The light (dark) shaded region refers, respectively, to the intersubband (intrasubband) SPE. The bold solid curve marked as ω^{00}_{mp} (ω^{10}_{mp}) is the intrasubband (intersubband) CME. Noticeable from the figure is the fact that all the SPE and CME observe a kind of *shoulder* exactly at $n_{1D}=1.006\times10^6$ cm^{-1}, corresponding to the similar shoulder in the Fermi energy for the same set of parameters. We observe that both intrasubband and intersubband CMEs increase with increasing charge density n_{1D}. At $n_{1D}\geqslant0.936\times10^6$ cm^{-1} the intrasubband CME propagates to remain inside the intersubband SPE. Both lower and upper edges of the intrasubband SPE are seen to increase with increasing charge density. The upper (lower) edge of the intersubband SPE increases (decreases) with increasing n_{1D} and both edges retain almost the same trend even after the shoulder. In the close vicinity of the shoulder, there is a short interval within which all the SPE and CME demonstrate a sort of independence of the charge density. We recall that similar behavior of plasmon spectrum was noticed in the absence of an applied magnetic field (see, e.g., Fig. 5 in Ref. 32). It is interesting to note that

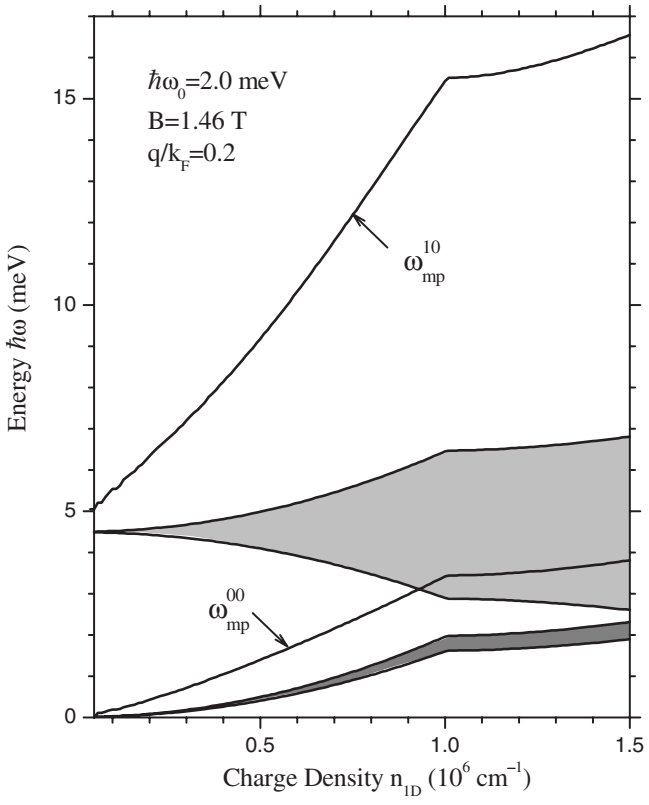

FIG. 12. Magnetoplasmon dispersion plotted as energy $\hbar\omega$ vs charge density n_{1D}, for the given values of $\hbar\omega_0$, B, and q_y/k_F. We take $\alpha=0$ in order to neglect the Rashba SOI. The light (dark) shaded region refers, respectively, to the intersubband (intrasubband) SPE. The bold solid curve marked as ω_{mp}^{00} (ω_{mp}^{10}) is the intrasubband (intersubband) CME. A kind of shoulder at $n_{1D}=1.006\times10^6$ cm^{-1}, both in CME and SPE, corresponds to the shoulder in the Fermi energy. The parameters are given inside the picture.

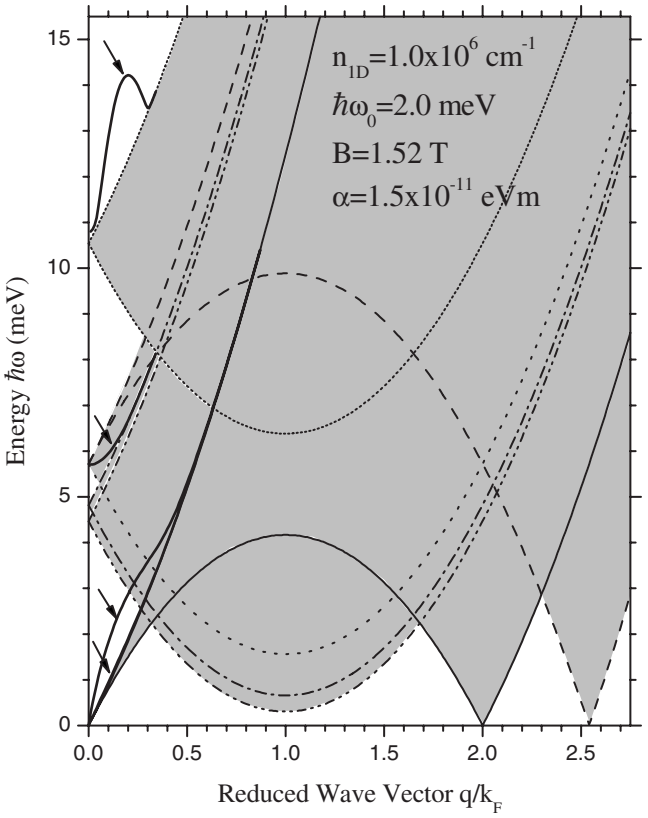

FIG. 13. Magnetoplasmon dispersion plotted as energy $\hbar\omega$ vs reduced wave vector q/k_F, for the given values of n_{1D}, $\hbar\omega_0$, B, and α. Here we take $\alpha\neq0$ in order to include the Rashba SOI. The shaded regions enclosed by pairs of identical lines (solid, dashed, dotted, dash-dotted, dash-dot-dotted, and short-dotted) refer to the different single-particle continua. The bold solid curves indicated by arrows are the collective (magnetoplasmon) excitations. The parameters are given inside the picture.

the intersubband CME remains free from Landau damping throughout and is therefore an observable long-lived collective excitation. This remark is equally valid for Fig. 11.

B. Magnetoplasmon dispersion with spin-orbit interaction (i.e., $\alpha\neq0$)

Figure 13 illustrates the magnetoplasmon dispersion for the Q1DEG with the Rashba SOI, for the given values of n_{1D}, $\hbar\omega_0$, B, and α. The shaded regions enclosed by pairs of identical lines (solid, dashed, dotted, dash-dotted, dash-dot-dotted, and short-dotted) refer to the different single-particle continua. The bold solid curves indicated by arrows are the collective (magnetoplasmon) excitations. Apparently there are four intersubband single-particle continua and one intrasubband SPE. Literally speaking, this is not true, because the SPE enclosed by dashed lines (and apparently originating from $\hbar\omega=5.72$ meV) is a mixed SPE having character of both intersubband and intrasubband SPEs. Look, for instance, at the short-dashed line with a minimum at $q_y/k_F=1.0$ and the dashed line ending up with a zero at $q_y/k_F=2.541$. The former gives an impression that it is an intersubband SPE and the latter tells us that it is an intrasubband SPE. The fact is that these three branches enclose an SPE region which emerges from the intrasubband SPE. Why then it looks like an intersubband SPE is simply because of the Rashba SOI term, which is, in a way, equivalent to a kind of subband spacing. Henceforth, we will call this region a mixed SPE. We now know it for certainty that the role of these single-particle continua is only to define whether or not a certain collective mode is Landau damped. Once a CME merges with the SPE it ceases to be a long-lived excitation and is Landau damped. We observe that there are two intrasubband CMEs and two intersubband CMEs indicated by the arrows. However, the lower intrasubband CME is not discernible from the upper edge of the intrasubband SPE and the lower intersubband CME that starts from within the mixed SPE propagates along the upper edge of the second lowest (counting from the bottom) SPE. Our understanding is that both of these CMEs are Landau damped throughout. Therefore, we are left with virtually two CMEs—the second lowest and the fourth lowest (counting from the bottom)—which are bonafide collective excitations until they merge with the respective SPE. The second-lowest CME starts at zero and merges with the upper edge of the intrasubband SPE (originating from zero) at ($q_y/k_F=0.71$, $\hbar\omega=8.02$ meV)

and becomes Landau damped. The fourth-lowest CME is, in fact, the magnetoroton, which starts at ($q_y/k_F=0$, $\hbar\omega=10.8$ meV), attains a maximum at ($q_y/k_F=0.2$, $\hbar\omega=14.22$ meV), reaches its roton minimum at ($q_y/k_F=0.3$, $\hbar\omega=13.5$ meV), and rises up to merge with the upper edge of the highest SPE at ($q_y/k_F=0.34$, $\hbar\omega=13.85$ meV).

While analytical diagnosis of the critical points of the CME is really a *hard nut to crack*, we can do so for the SPE. The lowest critical point on the x axis is $q_r=q_y/k_F=1$ where we have three minima. These are given by

$$\hbar\omega = \begin{cases} \epsilon_{21}^{--}\hbar\tilde{\omega} - \dfrac{\hbar^2k_F^2}{2m_r} = 0.3024 \text{ meV} \\ \epsilon_{21}^{++}\hbar\tilde{\omega} - \dfrac{\hbar^2k_F^2}{2m_r} = 0.6556 \text{ meV} \\ \tilde{\epsilon}_1\hbar\tilde{\omega} - \dfrac{\hbar^2k_F^2}{2m_r} = 1.5588 \text{ meV}. \end{cases} \quad (45)$$

Similarly, the second-lowest point on the x axis is $q_r=2$ where the lower branch of the intrasubband SPE goes to zero. It is obtained from the following expression:

$$\hbar\omega = \frac{\hbar^2k_F^2}{2m_r}q_r^2 - \frac{\hbar^2k_F^2}{m_r}q_r = 0. \quad (46)$$

The third-lowest point on the x axis is $q_r=2.541$ where (one of) the lower branch of the mixed SPE goes to zero. It is defined by

$$\hbar\omega = \frac{\hbar^2k_F^2}{2m_r}q_r^2 - \tilde{\epsilon}_1\hbar\tilde{\omega} - \frac{\hbar^2k_F^2}{m_r}q_r = 0. \quad (47)$$

Now, let us go the y axis. The lowest critical point on the y axis is where the lowest intersubband SPE (counting from the bottom) starts with and it is defined by

$$\hbar\omega = \epsilon_{21}^{--}\hbar\tilde{\omega} = 4.4635 \text{ meV}. \quad (48)$$

The second-lowest point on the y axis is where the second-lowest intersubband SPE starts with and it is given by

$$\hbar\omega = \epsilon_{21}^{++}\hbar\tilde{\omega} = 4.8167 \text{ meV}. \quad (49)$$

The third-lowest point on the y axis is where the mixed SPE starts with and it is defined by

$$\hbar\omega = \tilde{\epsilon}_1\hbar\tilde{\omega} = 5.7200 \text{ meV}. \quad (50)$$

The fourth-lowest critical point on the y axis is where the highest SPE starts with and it is given by

$$\hbar\omega = \epsilon_{21}^{-+}\hbar\tilde{\omega} = 10.5370 \text{ meV}. \quad (51)$$

Interestingly, Eqs. (45), (46), and (48)—with $\tilde{\epsilon}_1=\epsilon_{21}^{--}=\epsilon_{21}^{++}=1$—also reproduce exactly all three critical points of Fig. 9 in the absence of the Rashba SOI, as is expected. It is now natural to ask the following: What is the role played by the Rashba SOI in the magnetoplasmon dispersion? To answer the question requires us to take a comparative look at Figs. 9 and 13. This leads us to infer that the Rashba SOI pulls the intrasubband CME to a little longer life in the $\omega-q_y$ space. As to the magnetoroton, the Rashba SOI makes it to start at a little higher energy, it attains its maximum at lower q_y with lower energy, it reaches its minimum at lower q_y with higher energy, and it merges with the respective SPE at lower q_y with lower energy.

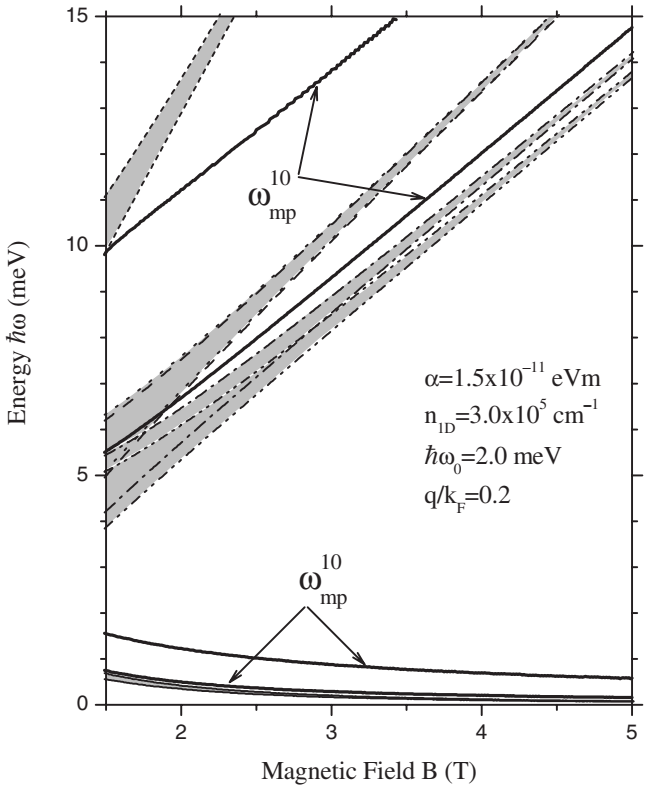

FIG. 14. Magnetoplasmon dispersion plotted as energy $\hbar\omega$ vs magnetic field B, for the given values of n_{1D}, $\hbar\omega_0$, q_y/k_F, and α. The shaded regions enclosed by pairs of identical lines (solid, dashed, dotted, dash-dotted, dash-dot-dotted, and short-dotted) refer to the different single-particle continua. The bold solid curves indicated by arrows are the collective (magnetoplasmon) excitations. The parameters are given inside the picture.

Figure 14 displays the magnetoplasmon dispersion as a function of the magnetic field for the realistic quantum wire, for a given value of n_{1D}, $\hbar\omega_0$, q_y/k_F, and α. The shaded regions enclosed by pairs of identical lines (solid, dashed, dotted, dash-dotted, dash-dot-dotted, and short-dotted) refer to the different single-particle continua. The bold solid curves indicated by arrows are the collective (magnetoplasmon) excitations. The collective excitations marked as ω_{mp}^{00} (ω_{mp}^{10}) refer to the intrasubband (intersubband) CME. Notice the scale on the x axis where we start from $B=1.5$ T, in order to avoid the lower values where the said inequality fails to hold good. There are four well-defined intermediate single-particle continua, which we call the mixed SPE. Both the lower and upper pairs of the mixed SPE are seen to overlap for $B\leqslant 1.78$ T and the lower pair is also observed to split at $B\simeq 2.99$ T. The upper and lower intrasubband CMEs start, respectively, at $\hbar\omega=1.54$ meV and $\hbar\omega=0.76$ meV. Both intrasubband CMEs show a negative energy dispersion, just as the pure (the lowest) intrasubband SPE, with increasing magnetic field. Note that although the lowest CME propagates in the close vicinity of the upper edge of the intrasubband SPE,

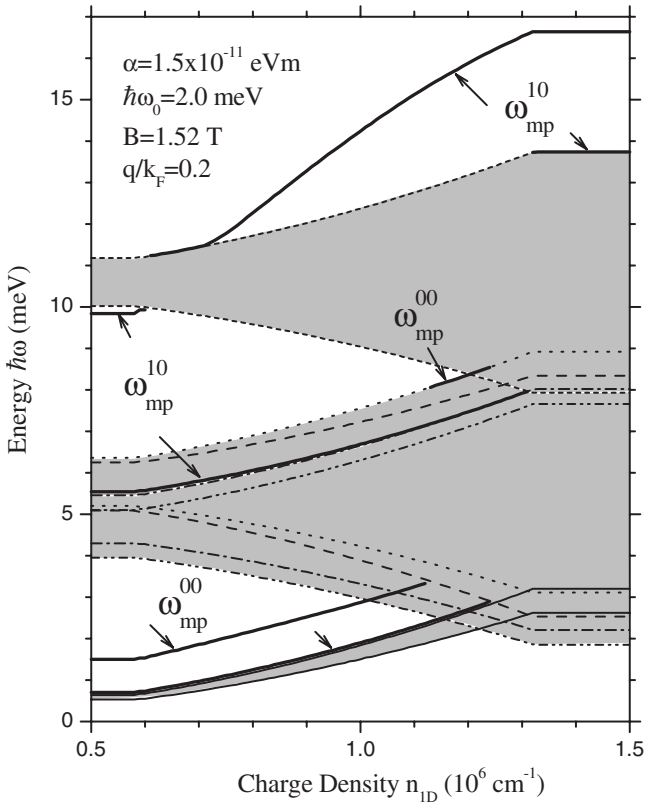

FIG. 15. Magnetoplasmon dispersion plotted as energy $\hbar\omega$ vs charge density n_{1D}, for the given values of $\hbar\omega_0$, B, q_y/k_F, and α. The shaded regions enclosed by pairs of identical lines (solid, dashed, dotted, dash-dotted, dash-dot-dotted, and short-dotted) refer to the different single-particle continua. The bold solid curves indicated by arrows and marked as ω_{mp}^{00} (ω_{mp}^{10}) are the intrasubband (intersubband) collective excitations. A kind of shoulder at $n_{1D}=1.329\times10^6$ cm^{-1}, both in CME and SPE, corresponds to the shoulder in the Fermi energy. The parameters are given inside the picture.

it nevertheless remains quite discernible throughout. The highest intersubband CME emerges from the lower edge of the highest intersubband SPE at $\hbar\omega=9.81$ meV to propagate within the gap between the upper pair of mixed SPE and the highest intersubband SPE. The lower intersubband CME starts at $\hbar\omega=5.55$ meV from the uppermost edge of the lower pair of the mixed SPE, within the region where lower and upper pairs of the mixed SPE overlap. Finally, it emerges from the lowest edge of the upper pair of the mixed SPE at $B=1.95$ T to propagate within the gap between the lower and upper pairs of the mixed SPE. The wide energy gaps both above and below the mixed SPE, as well as the one between the mixed pairs of SPE, are noteworthy. The physical significance of these gaps is that they guarantee that all the collective magnetoplasmons are Landau undamped, long-lived, bonafide, and easily observable modes. The only exception to this is the small region (below $B\leqslant1.78$ T) associated with the emergence of the lower intersubband CME.

Figure 15 shows the magnetoplasmon dispersion as a function of the 1D charge density n_{1D} for the realistic quantum wire, for the given values of $\hbar\omega_0$, B, q_y/k_F, and α. The shaded regions enclosed by pairs of identical lines (solid, dashed, dotted, dash-dotted, dash-dot-dotted, and short-dotted) refer to the different single-particle continua. The bold solid curve indicated by arrows and marked as ω_{mp}^{00} (ω_{mp}^{10}) are the intrasubband (intersubband) collective excitations. A kind of shoulder at $n_{1D}=1.329\times10^6$ cm^{-1}, both in CME and SPE, corresponds to the shoulder in the Fermi energy. The four well-defined intermediate single-particle continua are now gapless, unlike Fig. 14. The energy of both intrasubband CMEs increases with increasing charge density. The lower CME propagates along the upper edge of the intrasubband SPE and stops just at the lower edge of the intermediate SPE enclosed by the dashed lines. The upper CME also stops at the lower edge of the same SPE but emerges at the upper edge of the SPE enclosed by the short-dashed lines at ($n_{1D}=1.13\times10^6$ cm^{-1}, $\hbar\omega=8.06$ meV) to stop again at ($n_{1D}=1.24\times10^6$ cm^{-1}, $\hbar\omega=8.54$ meV). The lower intersubband CME starts just above the upper edge of the intermediate SPE enclosed by the dash-dotted lines and stops at the lower edge of the highest SPE at ($n_{1D}=1.31\times10^6$ cm^{-1}, $\hbar\omega=7.96$ meV but emerges at the upper edge of the highest SPE at $n_{1D}=1.32\times10^6$ cm^{-1}, $\hbar\omega=13.73$ meV) to propagate along that same edge. The upper intersubband CME starts just below the lower edge of the highest SPE, stops at ($n_{1D}=0.60\times10^6$ cm^{-1}, $\hbar\omega=9.93$ meV), but emerges at ($n_{1D}=0.61\times10^6$ cm^{-1}, $\hbar\omega=11.24$ meV) to propagate with the energy increasing with charge density. The (almost) nondispersive part of the spectrum, after the shoulder, is again dictated by the Fermi energy for the set of parameters used.

Figure 16 shows the magnetoplasmon dispersion as a function of the Rashba parameter α for the realistic quantum wire, for the given values of n_{1D}, $\hbar\omega_0$, B, and q_y/k_F. The bold solid curves indicated by arrows and marked as 00 (10) are the intrasubband (intersubband) collective excitations. Again, we observe four well-defined intermediate single-particle continua and no discontinuity in the propagation of the collective excitations, unlike Figs. 14 and 15. The two intrasubband CMEs start at $\hbar\omega=1.92$ meV and $\hbar\omega=2.87$ meV and end up, respectively, at $\hbar\omega=1.84$ meV and $\hbar\omega=2.85$ meV. This means that both modes are almost dispersionless in the entire range of α. It is important to note that the lower intrasubband CME starts just above the upper edge of the intrasubband SPE and finally merges with the same edge. This implies that it may be an observable mode until it merges with the respective SPE. The lower intersubband CME starts just above the upper edge of the intermediate SPE enclosed by the dashed lines, crosses this edge at ($\alpha=0.471\times10^{-11}$ eV m, $\hbar\omega=6.894$ meV), to merge with (at $\alpha=1.9\times10^{-11}$ eV m, $\hbar\omega=6.75$ meV) and propagate along with the upper edge of the SPE enclosed by the dash-dotted lines. The upper intersubband CME starts at ($\alpha=0.10\times10^{-11}$ eV m, $\hbar\omega=14.26$ meV) and propagates along the upper edge of the highest SPE but does not quite merge with it. This implies that the lower intrasubband CME (until it merges with the upper edge of the SPE), the upper intrasubband CME (until it merges with the lower edge of the SPE enclosed by the dash-dot-dotted line), and the upper intersubband CME are all bonafide observable collective excitations.

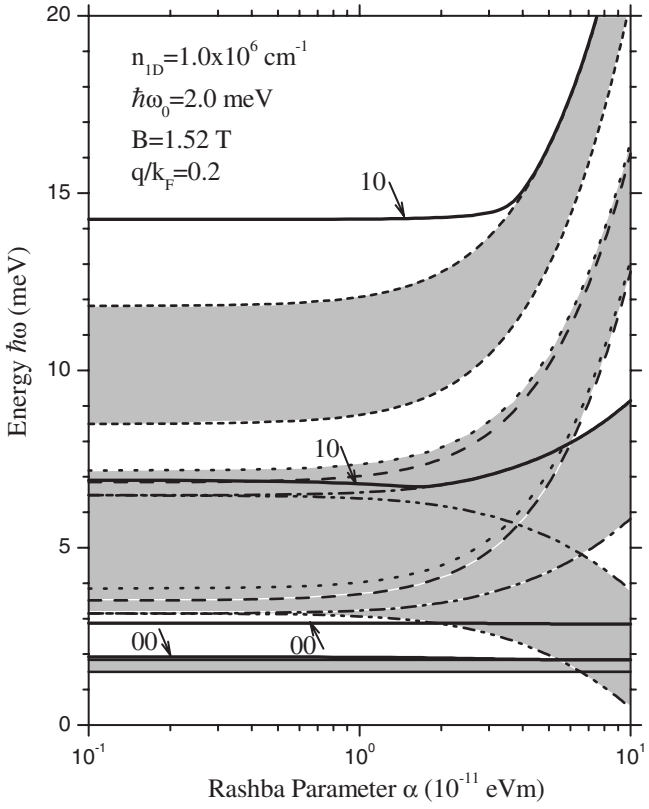

FIG. 16. Magnetoplasmon dispersion plotted as energy $\hbar\omega$ vs Rashba parameter α, for the given values of n_{1D}, $\hbar\omega_0$, B, and q_y/k_F. The shaded regions enclosed by pairs of identical lines (solid, dashed, dotted, dash-dotted, dash-dot-dotted, and short-dotted) refer to the different single-particle continua. The bold solid curves indicated by arrows and marked as 00 (10) are the intrasubband (intersubband) collective excitations. The parameters are given inside the picture.

C. On the Bernstein modes

A difficulty with the characterization of narrow channels is how to determine the electron density and the width. Ideally, a quantal simulation based on a combined, self-consistent solution of the Schrödinger and Poisson equations for the test structure should answer this question. In practice, however, this procedure is complicated by numerous uncontrolled factors introduced during the fabrication process, such as damage-related traps and deep impurities. In order to let the theoretical model function quantitatively, one is bound to specify the shape of the confining potential. The quantal simulations may fail in this context in predicting the correct carrier concentration, etc., but should nevertheless give a realistic idea about the shape of the confining potential. Thus simulations for split-gate GaAs/$Ga_{1-x}Al_xAs$ heterostructure suggest a potential which is approximately harmonic for very narrow channels.[39] For wider channels the potential shape is somewhere between that of a harmonic potential and a square well.[1]

Another important issue is that the many-body effects become more and more important as the system's dimensions diminish[1] and the interactions can have important effects on the magnetic-field dependence of the energy spectrum. However, it is also becoming widely known that, when the confining potential is harmonic, the far-infrared spectroscopy is insensitive to the interaction effects because the optical excitations are then the excitations of the center-of-mass (c.m.) motion and have exactly the same energies as the single-electron excitations. Theoretically, the Hamiltonian in this situation separates into two parts: one corresponds to the c.m. motion and the other to the relative motion. This is a very special property of harmonic potential; had the shape of the confining potential been different, the c.m. motion would couple to the relative motion. To be brief, this is a manifestation of the Kohn theorem[21] generalized to harmonically confined quantum wells,[40] quantum wires,[41] and quantum dots.[42] The *generalized* Kohn's theorem states that in an ideal parabolic potential the absorption spectrum is not only independent of the electron-electron interaction, but also independent of the electron density in the system.

In various papers on quantum wells, wires, and dots, another type of interaction has been observed,[1] which occurs at or near the crossing of, e.g., wire modes with the harmonics $n\omega_c$ (with $n \geqslant 2$) of the cyclotron frequency. These interactions resemble the so-called Bernstein modes,[43] which have been observed in three-dimensional electron system (3DES),[44] 2DES,[45] and one-dimensional electron system (1DES).[46] Excitations of harmonics of the cyclotron resonance are strictly forbidden in an isotropic, translationally invariant electron system with a parabolic band structure. However, the dynamic spatial modulation of the charge density of a plasmon breaks the isotropy and causes a strong interaction. This leads to an *anticrossing* when the magnetoplasmon dispersion crosses harmonics $n\omega_c$ ($n \geqslant 2$) of the cyclotron frequency. This $n\omega_c$ splitting of the magnetoplasmon dispersion in a 2DES, both with and without the Rashba SOI, was recently reported by the author.[31] The strength of the splitting is governed by the parameter $(qv_F/\omega_c)^2$ where q is the wave vector of the magnetoplasmon and v_F is the Fermi velocity. The very appearance of v_F in the parameter emphasizes its pure quantum origin. Thus the interaction of the magnetoplasmons with the harmonics of the cyclotron frequency cannot be observed in classical models (based on, e.g., electrodynamics or hydrodynamics).

Figure 17 illustrates the Bernstein modes within a six-subband model—with only the lowest one occupied—occurring at $n\tilde{\omega}$ (with $n=1,2,3,\ldots$). The question is the following. What happens to the relevant (naturally, the intersubband) magnetoplasmons exhibiting the *anticrossings* at or near the $n\tilde{\omega}$? The answer to the question lies in the above discussion itself. We do not observe any *anticrossing* with the Bernstein modes [in the *long-wavelength* limit (LWL)] because our model potential is an ideal harmonic potential wherein such an interaction is quenched. The splittings in question arise if and only if the system is subjected to a strong *anharmonic* potential, i.e., when the resultant confining potential deviates strongly from the parabolic one. In addition, in order to observe the said splittings more than one Landau band has to be occupied. However, Fig. 17 demonstrates that the Bernstein modes are the general phenomena observable not only in 3DES and 2DES but also in 1DES. In the LWL and strong magnetic field, the broadened

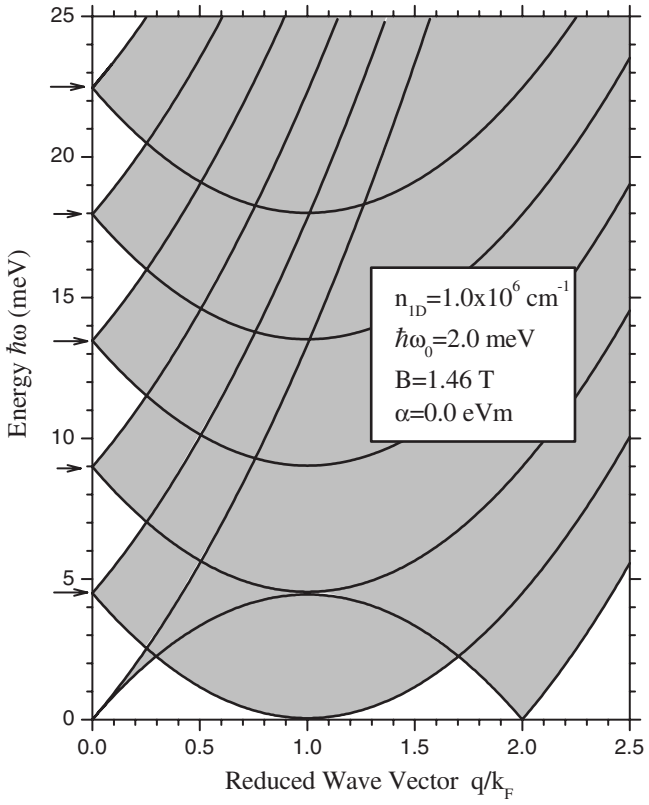

FIG. 17. Single-particle excitation spectrum plotted as energy $\hbar\omega$ vs reduced wave vector q/k_F within a six-subband model, for the given values of n_{1D}, $\hbar\omega_0$, and B. Here we take $\alpha=0$ in order to neglect the Rashba SOI. The shaded regions are merely the single-particle continua which appear in the long-wavelength limit at $n\hbar\tilde{\omega}$, $n=1,2,3,\ldots$. The parameters are given inside the picture.

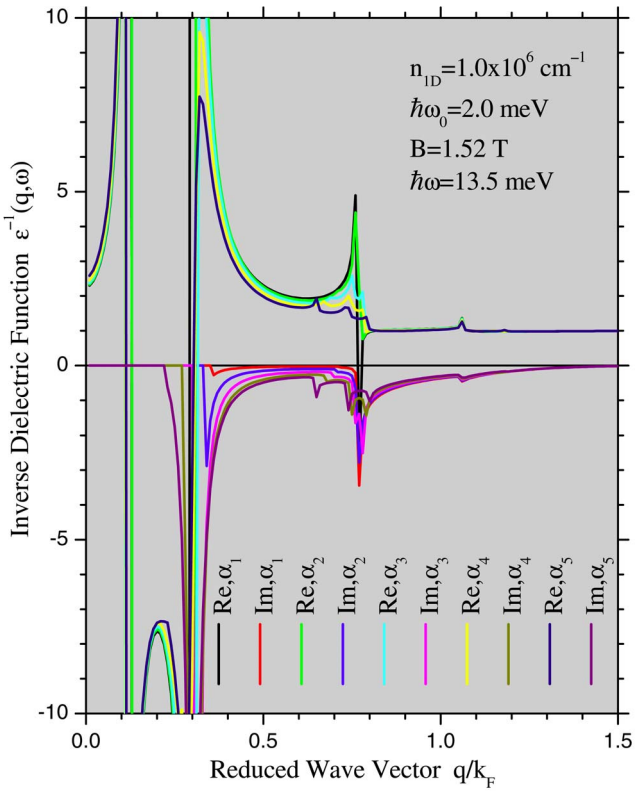

FIG. 18. (Color online) Inverse dielectric function $\epsilon^{-1}(q_y,\omega)$ versus reduced wave vector q_y/k_F, for the given values of the Rashba parameter α. The symbol R (I) refers to real (imaginary) part of the dielectric function. Here $\alpha_1=0.5\times10^{-11}$ eV m, $\alpha_2=1.0\times10^{-11}$ eV m, $\alpha_3=1.5\times10^{-11}$ eV m, $\alpha_4=2.0\times10^{-11}$ eV m, and $\alpha_5=2.5\times10^{-11}$ eV m. The other parameters are given inside the picture.

SPEs in Fig. 17 show up diminishingly thin stripes with (almost) zero thickness near $q_y=0$. These are the resonant modes termed as Bernstein modes which appear in the present case at $n\tilde{\omega}$.

D. Inverse dielectric function $\epsilon^{-1}(q,\omega)$

It is now becoming known that spintronics is richer in semiconductors than in metals because doping, gating, and heterojunction formation can be exploited to tailor the key material properties and because of the intimate relationship between optical and transport properties in semiconductors. In view of this, we also studied briefly the inverse (nonlocal, dynamic) dielectric function $[\epsilon^{-1}(q_y,\omega)]$, which is closely related to the longitudinal and transverse (Hall) resistances in such realistic Q1D quantum wires. For instance, the longitudinal (Hall) resistance ρ_{xx} (ρ_{xy}) is determined by the imaginary (real) part of the inverse dielectric function. Such an investigation is worthwhile because it would allow us to use the transport measurements to probe the reactive (real) part of the inverse dielectric function.

Figure 18 illustrates the inverse dielectric function $\epsilon^{-1}(q_y,\omega)$ as a function of the reduced wave vector q_y/k_F, for the given values of the Rashba parameter α. It should be pointed out that the quantity that directly affects the transport is the spectral weight $\mathrm{Im}[\epsilon^{-1}(q_y,\omega)]$, which contains both the single-particle contribution at large q_y and the collective (magnetoplasmon) contribution at small q_y. It is clearly observed that the sharp peaks at the reduced wave vector $q_y/k_F=0.12$ and 0.3 stand for the two positions of the magnetoroton for the given energy $\hbar\omega=13.5$ meV (see, e.g., Fig. 13) and the broader peaks at $q_y/k_F\simeq0.31$, 0.69, 0.75, 0.79, and 1.06 refer exactly to the respective intersubband SPE; the first of them is exactly when the roton mode merges with the closest (and highest) SPE. Clearly, these peaks are a result of the existing poles of the inverse dielectric function at the corresponding values of $\hbar\omega$ and q_y. Due to Rashba spin splitting, there are numerous momentum transfers for a given energy $\hbar\omega$: intra-$[(^{+-}_{11})$ and $(^{-+}_{11})]$ and inter-$[(^{++}_{21})$, $(^{--}_{21})$, $(^{+-}_{21})$, $(^{-+}_{21})]$ spin-channel transitions. This gives rise to the fine structures in both the real and imaginary parts of $\epsilon^{-1}(q_y,\omega)$. These fine structures are, however, vividly resolved only when the Rashba parameter α characterizing the SOI is sufficiently large. In the present situation, such structures are seen, for instance, for $\alpha=1.5\times10^{-11}$, 2.0×10^{-11}, and 2.5×10^{-11} eV m.

We believe that such fine structures should also be mimicked in the plots of the longitudinal (ρ_{xx}) and transverse (ρ_{xy}) resistances plotted as a function of energy. It is note-

worthy that the quantity $\mathrm{Im}[\epsilon^{-1}(q_y,\omega)]$ also implicitly provides the details of the Raman (or electron) scattering cross-section $S(q_y)$ in the system.[29] Thus ρ_{xx} can also be understood as a weighted sum of the scattering cross section. As such, we expect that the main effect of the Rashba spin splitting is to redistribute the scattering probability at different q_y but not to significantly change the total cross section summed over all q_y. Extensive details of the study of ρ_{xx} and ρ_{xy} are deferred to a future publication.

IV. CONCLUDING REMARKS

In summary, we have investigated extensively the magnetoplasmons in a Q1DEG in the presence of the Rashba spin-orbit interactions in the framework of an exact standard RPA (without following any perturbative approach) within a two-subband model. The elementary characterization of the quantum wire by studying, e.g., the single-particle eigenenergies (both with and without the magnetic field), the density of states, the nonlinear Landau fan diagram, the magnetic depopulation of hybrid magnetoelectric subbands, the Fermi energies (both with and without the Rashba SOI), and the magnetic-field dependence of the crucial parameters such as δ and $\tilde{\epsilon}_n$ involved in the theory is followed by the principal results on the magnetoplasmon dispersion both with and without the Rashba SOI.

In the absence of the SOI, we recover two important and unique characteristics of Q1DEG (subjected to an applied perpendicular magnetic field): (1) the negative-B dispersion of the intrasubband magnetoplasmon and (2) the intersubband magnetoplasmon that manifests the character of a magnetoroton showing up a maximum and a minimum before merging with the respective SPE. A systematic evolution of the magnetoroton with the magnetic field is shown. The excitation spectrum displaying energy versus the charge density reflects a kind of shoulder corresponding to a similar structure in the Fermi energy.

The presence of the Rashba SOI makes the magnetoplasmon spectrum richer but complex. We studied the excitation spectrum as a function of the propagation vector, the magnetic field, 1D charge density, and the Rashba parameter characterizing the SOI. The q_y dependence of the spectrum (Fig. 13) leads us to infer the following: (1) the presence of the α term creates additional single-particle continua which are obviously dangerous to the collective (magnetoplasmon) excitations, (2) we observe four CMEs but the second lowest and the fourth lowest (i.e., the magnetoroton) are expected to be the only bonafide CME observable in the experiment, (3) the magnetoroton minimum (maximum) goes up (down) in energy and both maxon and roton shift toward lower q_y, and, most importantly, (4) the Rashba SOI seems to suppress the depolarization shift (cf, Figs. 9 and 13). The B dependence (Fig. 14) reveals that there are four (two intra- and two intersubbands) CMEs in the range specified by $B \gtrsim 1.87$ T for $q_y/k_F=0.2$ and all are Landau undamped and hence long-lived excitations. It is noteworthy that the B dependence (Fig. 14) was computed only for the spin-down channels which observe the magnetic depopulation. For other situations (e.g., for the spin-up channels and/or the considering both channels together) the spectrum is far too complicated to digest. This also leads us to think that the negative-B dispersion of the intrasubband CME (with or without the Rashba SOI) is possibly a consequence of the magnetic depopulation of the subbands. The n_{1D} dependence (Fig. 15) let us believe that the upper intrasubband and the upper intersubband CMEs are the only bonafide collective excitations observable in the experiment. The α dependence (Fig. 16) is relatively much smoother and speaks more clearly than the B and n_{1D} dependences. It shows how both intrasubband and intersubband CMEs and SPEs are dispersionless for $\alpha \lesssim 1.0\times10^{-11}$ eV m, and with the upper intrasubband and the upper intersubband CMEs as the only modes detectable in the experiments. We have also shown (Fig. 17) that the Q1DEG can support the Bernstein (or the resonant) modes occurring at $n\tilde{\omega}$.

A study of the inverse dielectric function (Fig. 18) leads us to substantiate the magnetoplasmon modes searched with the zeros of the dielectric function. This is what we should anticipate because searching the zeros of the dielectric function and the poles of the inverse dielectric function must yield exactly identical results. Moreover, studying the influence of α on the inverse dielectric function provides us with important information on the effect of the Rashba SOI on the longitudinal and Hall resistances. The imaginary part of the inverse dielectric function also furnishes significant estimates of the Raman (or electron) scattering cross section.

Finally, we believe that the present investigation of the plasmon excitations in a Q1DEG in the presence of a magnetic field and the Rashba SOI is of experimental importance to the emerging field of semiconductor spintronics. Considering a confining potential that deviates from the parabolic form and including the many-body effects could give better insight into the problem. We hope that such behavior characteristics of the magnetoplasmons as studied and predicted here can be verified by the Raman scattering experiments. Currently, we have been studying the effect of the Rashba SOI on the magneto-optics of a many-electron quantum dot in the presence of a perpendicular magnetic field and the results will be reported shortly.

A cautionary remark. We recall a well-known fact in the history of science that no mathematical *inequality* is ever known to impose a *sharp* boundary between the valid and the invalid regimes of a certain physical quantity. Here this quantity is the magnetic field B. We have noticed that even the moderate magnetic field ($l_0/l_c=\sqrt{2} \Rightarrow B \simeq 1.45$ T) does not violate the obtension of the JC model (with no anticrossings, at least for the lowest subband model as is the case here; see, e.g., the lowest panel of Fig. 2). As regards Figs. 2, 6, and 8, they do not represent any collective effects and the question of validity of the said inequality (for $0 \leqslant B \leqslant 1.45$ T, i.e., within the shaded region) is of much less importance. However, if we stick to the *principle* then we must (simply) ignore this weaker regime [the shaded region(s) in the aforesaid figures] where the said inequality does not hold good. And we are just as safe as we ought to be.

ACKNOWLEDGMENTS

The author has enjoyed very fruitful communications and

discussions with Godfrey Gumbs and Sergio Ulloa. This work was partially supported by CONACyT Grant No. SEP-2003-C02-42761.

APPENDIX: STRATEGY OF SEARCHING SOLUTIONS OF EQUATION (3)

Making use of the Hermite functions (with the center of the cyclotron orbit lying at x_c) in the absence of any Rashba SOI as the basis, we express the eigenfunction in the following form:

$$\phi_{\uparrow\downarrow}(x) = \frac{1}{\sqrt{L_y}} \sum_{n\sigma} \phi_n(x+x_c) C_n^{\sigma} |\sigma\rangle = \frac{1}{\sqrt{L_y}} \sum_{n} \phi_n(x+x_c) \begin{pmatrix} C_n^{+} \\ C_n^{-} \end{pmatrix}, \tag{A1}$$

where the symbols used have already been defined in the text and the function $\phi_n(x)$ is the Hermite function specified in Eq. (10) in the text. Here $|\sigma\rangle$ stands for the electron spin written as a column vector $|\sigma\rangle = \binom{1}{0}$ for spin up and $|\sigma\rangle = \binom{0}{1}$ for spin down. Remember, we start working with both signs (or arrows) together in Eq. (3). The result of using Eq. (A1) in Eq. (3), multiplying the resulting equation by $\phi_m(x+x_c)$, and integrating over z is

$$\sum_n \int \left(\left\{ l_0^2 \phi_n''(z)\phi_m(z) + \left[\epsilon_x^{\pm} - \frac{a}{l_0^2}(z-x_c)^2 - \frac{b}{l_0}(z-x_c) \right] \phi_n(z)\phi_m(z) \right\} \begin{pmatrix} C_n^{+} \\ C_n^{-} \end{pmatrix} - \left\{ \pm \frac{l_0^2}{l_\alpha} \phi_n'(z)\phi_m(z) + \frac{l_0}{l_\alpha} \left[\left(\frac{l_0}{l_c} \right)^2 \frac{1}{l_0}(z-x_c) + k_y l_0 \right] \phi_n(z)\phi_m(z) \right\} \begin{pmatrix} C_n^{-} \\ C_n^{+} \end{pmatrix} \right) dz = 0 \tag{A2}$$

where we have substituted $z = x + x_c$ for the sake of brevity. Next, substitute $z = l_d y$, with y a dimensionless quantity, evaluate ϕ_n' and ϕ_n'' with the aid of Eq. (10) and making use of the recurrence relations for the Hermite polynomials,[38] and solve the resulting integrals involving a product of two Hermite polynomials with different indices[38] to finally determine each of the *seven* terms involved in Eq. (A2). Note that by this moment we have made absolutely *no* approximation at all. Now, we make careful use of the strong-field-limit $l_c \ll l_0$ (and $k_y l_0 \ll 1$) to obtain a set of two decoupled equations written as follows:

$$\left[\epsilon_x^{+} - \left(\frac{l_0}{l_d} \right)^2 (2n+1) + (k_y l_0)^2 \left(\frac{l_d}{l_c} \right)^4 \right] C_n^{+} - \frac{l_0^2}{l_\alpha l_d} \frac{S}{\sqrt{2}} \sqrt{n+1} C_{n+1}^{-} = 0, \tag{A3}$$

$$\left[\epsilon_x^{-} - \left(\frac{l_0}{l_d} \right)^2 (2n+1) + (k_y l_0)^2 \left(\frac{l_d}{l_c} \right)^4 \right] C_n^{-} - \frac{l_0^2}{l_\alpha l_d} \frac{S}{\sqrt{2}} \sqrt{n} C_{n-1}^{+} = 0. \tag{A4}$$

Equations (A3) and (A4) can also be conveniently written as

$$\left[\epsilon_y^{+} - \left(\frac{l_0}{l_d} \right)^2 (2n-1) \right] C_{n-1}^{+} - \frac{l_0^2}{l_\alpha l_d} \frac{S}{\sqrt{2}} \sqrt{n} C_n^{-} = 0, \tag{A5}$$

$$- \frac{l_0^2}{l_\alpha l_d} \frac{S}{\sqrt{2}} \sqrt{n} C_{n-1}^{+} + \left[\epsilon_y^{-} - \left(\frac{l_0}{l_d} \right)^2 (2n+1) \right] C_n^{-} = 0, \tag{A6}$$

where

$$\epsilon_y^{\pm} = \epsilon_x^{\pm} + k_y^2 l_0^2 (l_d^4/l_c^4),$$

$$\epsilon_x^{\pm} = \epsilon_x \mp \gamma (l_0^2/l_c^2). \tag{A7}$$

Imposing the condition of nontrivial solutions on this set of equations [Eqs. (A5) and (A6)] yields the eigenvalues given in Eq. (9). Similarly, solving the same set of equations systematically yields the eigenfunctions given by Eqs. (7) and (8) in the text.

[1] For an extensive review of electronic, optical, and transport properties of systems of reduced dimensions, such as quantum wells, wires, dots, and modulated 2D systems, see M. S. Kushwaha, Surf. Sci. Rep. **41**, 1 (2001).

[2] For a recent review of the field of spintronics, see I. Zutic, J. Fabian, and S. Das Sarma, Rev. Mod. Phys. **76**, 323 (2004).

[3] S. Datta and B. Das, Appl. Phys. Lett. **56**, 665 (1990).

[4] E. I. Rashba, Sov. Phys. Solid State **2**, 1109 (1960); Yu. A. Bychkov and E. I. Rashba, JETP Lett. **39**, 78 (1984); E. I. Rashba and Al. L. Efros, Phys. Rev. Lett. **91**, 126405 (2003).

[5] R. E. Dunin-Borkowski, M. R. McCartney, R. B. Frankel, D. A. Bazylinski, M. Posfai, and P. R. Buseck, Science **282**, 1868 (1998).

[6] B. E. Kane, Nature (London) **393**, 133 (1998).

[7] J. Nitta, F. E. Meijer, and H. Takayanagi, Appl. Phys. Lett. **75**, 695 (1999).

[8] T. Koga, J. Nitta, H. Takayanagi, and S. Datta, Phys. Rev. Lett. **88**, 126601 (2002).

[9] B. A. Gurney, in *Ultrathin Magnetic Strctures IV*, edited by B. Heinrich and J. A. C. Bland (Springer, Berlin, 2005), p. 149.

[10] R. Winkler, *Spin-Orbit Coupling Effects in Two-Dimensional Electron and Hole Systems* (Springer, New York, 2003).

[11] K. F. Berggren, T. J. Thornton, D. J. Newson, and M. Pepper, Phys. Rev. Lett. **57**, 1769 (1986).

[12] G. Timp, A. M. Chang, P. Mankiewich, R. Behringer, J. E. Cunningham, T. Y. Chang, and R. E. Howard, Phys. Rev. Lett. **59**, 732 (1987).

[13] M. L. Roukes, A. Scherer, S. J. Allen, Jr., H. G. Craighead, R. M. Ruthen, E. D. Beebe, and J. P. Harbison, Phys. Rev. Lett. **59**, 3011 (1987).

[14] B. J. van Wees, H. van Houten, C. W. J. Beenakker, J. G. Williamson, L. P. Kouwenhoven, D. van der Marel, and C. T. Foxon, Phys. Rev. Lett. **60**, 848 (1988).

[15] T. Demel, D. Heitmann, P. Grambow, and K. Ploog, Phys. Rev. Lett. **66**, 2657 (1991).

[16] A. R. Goñi, A. Pinczuk, J. S. Weiner, B. S. Dennis, L. N. Pfeiffer,

and K. W. West, Phys. Rev. Lett. **70**, 1151 (1993).
[17] O. M. Auslaender, H. Steiberg, A. Yacoby, Y. Tserkovnyak, B. I. Halperin, K. W. Baldwin, L. N. Pfeiffer, and K. W. West, Science **308**, 88 (2005). This is an experimental proof of the spin-charge separation [predicted by E. H. Leib and F. Y. Wu, Phys. Rev. Lett. **20**, 1445 (1968)] observed in the ballistic, parallel quantum wires in GaAs/AlGaAs heterostructure.
[18] Q. P. Li and S. Das Sarma, Phys. Rev. B **44**, 6277 (1991).
[19] S. R. Eric Yang and G. C. Aers, Phys. Rev. B **46**, 12456 (1992).
[20] L. Wendler and V. G. Grigoryan, Phys. Rev. B **49**, 13607 (1994).
[21] Walter Kohn, Phys. Rev. **123**, 1242 (1961), see also Ref. 1.
[22] A. V. Moroz and C. H. W. Barnes, Phys. Rev. B **61**, R2464 (2000).
[23] J. Wang, H. B. Sun, and D. Y. Xing, Phys. Rev. B **69**, 085304 (2004).
[24] S. Debald and B. Kramer, Phys. Rev. B **71**, 115322 (2005).
[25] S. Bellucci and P. Onorato, Phys. Rev. B **73**, 045329 (2006).
[26] Th. Schäpers, J. Knobbe, and V. A. Guzenko, Phys. Rev. B **69**, 235323 (2004).
[27] G. Fasol and H. Sakaki, Appl. Phys. Lett. **62**, 2230 (1993).
[28] B. E. Kane, Nature (London) **393**, 133 (1998).
[29] D. Pines and P. Nozieres, *The Theory of Quantum Liquids* (Benjamin, New York, 1966); A. L. Fetter and J. D. Walecka, *Quantum Theory of Many-Particle Systems* (McGraw-Hill, New York, 1971); G. D. Mahan, *Many Particle Physics* (Plenum, New York, 1981).
[30] M. S. Kushwaha and S. E. Ulloa, Phys. Rev. B **73**, 205306 (2006), and references therein.
[31] Manvir S. Kushwaha, Phys. Rev. B **74**, 045304 (2006).
[32] M. S. Kushwaha and S. E. Ulloa, Phys. Rev. B **73**, 045335 (2006).
[33] D. B. Mast, A. J. Dahm, and A. L. Fetter, Phys. Rev. Lett. **54**, 1706 (1985); Ch. Sikorski and U. Merkt, *ibid.* **62**, 2164 (1989); T. Demel, D. Heitmann, P. Grambow, and K. Ploog, *ibid.* **64**, 788 (1990).
[34] R. P. Feynman, *Statistical Mechanics* (W. A. Benjamin, Reading, MA, 1972).
[35] L. Allen and J. H. Eberly, *Optical Resonance and Two-Level Atoms* (Wiley, New York, 1975).
[36] E. T. Jaynes and F. W. Cummings, Proc. IEEE **51**, 89 (1963).
[37] M. Pletyukhov and O. Zaitsev, J. Phys. A **36**, 5181 (2003).
[38] I. S. Gradshteyn and I. M. Ryzhik, *Tables of Integrals, Series, and Products* (Academic, New York, 1994).
[39] S. E. Laux, D. J. Frank, and F. Stern, Surf. Sci. **196**, 101 (1988).
[40] L. Brey, N. F. Johnson, and B. I. Halperin, Phys. Rev. B **40**, 10647 (1989).
[41] Q. P. Li, K. Karrai, S. K. Yip, S. Das Sarma, and H. D. Drew, Phys. Rev. B **43**, 5151 (1991).
[42] F. M. Peeters, Phys. Rev. B **42**, 1486 (1990).
[43] Ira B. Bernstein, Phys. Rev. **109**, 10 (1958).
[44] C. K. N. Patel and R. E. Slusher, Phys. Rev. Lett. **21**, 1563 (1968).
[45] E. Batke, D. Heitmann, J. P. Kotthaus, and K. Ploog, Phys. Rev. Lett. **54**, 2367 (1985).
[46] C. Steinebach, R. Krahne, G. Biese, C. Schüller, D. Heitmann, and K. Eberl, Phys. Rev. B **54**, R14281 (1996).